Available online at www.sciencedirect.com
SCIENCE DIRECT®
Journal of Computational Physics 187 (2003) 457–491
JOURNAL OF COMPUTATIONAL PHYSICS
www.elsevier.com/locate/jcp

Solving elastodynamics in a fluid–solid heterogeneous sphere: a parallel spectral element approximation on non-conforming grids

Emmanuel Chaljub [a,b,*,1], Yann Capdeville [a,2], Jean-Pierre Vilotte [a]

[a] *Département de Sismologie and Département de Modélisation Physique et Numérique, Institut de Physique du Globe de Paris, 4 Place Jussieu, 75252 Paris Cedex 05, France*
[b] *Department of Geosciences, Princeton University, Princeton, NJ 08540, USA*

Received 14 March 2002; received in revised form 17 February 2003; accepted 18 February 2003

Abstract

We present a spectral element approach for modeling elastic wave propagation in a solid–fluid sphere where the local effects of gravity are taken into account. The equations are discretized in terms of the displacement in the solid and the velocity potential in a neutrally stratified fluid. The spatial approximation is based upon a spherical mesh of hexahedra in which local refinement allows for adapting the discretization to the variation of elastic parameters in both the solid and the fluid regions. Continuity constraints across the non-conforming interfaces are introduced through Lagrange multipliers which are further discretized by the mortar element method. Due to the spherical nature of the non-conforming interfaces the mortar method turns out to be functionally conforming and allows for an equal-order interpolation of the primal variables and the Lagrange multipliers. The method is shown to provide an accurate solution when compared to analytical calculations obtained for radial models of elastic parameters. Its parallel implementation is based upon a simple domain decomposition strategy which makes it efficient to solve large problems as those imposed by planetary scales.

Keywords: Computational seismology; Gravito-elastodynamics; Solid–fluid coupling; Spectral element method; Mortar element method; Spherical geometry; Gnomic projection; Hexahedral grid; Domain decomposition

1. Introduction

In global seismology, the development of accurate and computationally efficient methods to model elastic wave propagation is a challenging issue. In the past two decades, recorded arrival times and

* Corresponding author.
E-mail addresses: Emmanuel.Chaljub@obs.ujf-grenoble.fr (E. Chaljub), yann@seismo.berkeley.edu (Y. Capdeville), vilotte@ipgp.jussieu.fr (J.-P. Vilotte).
[1] Present address: LGIT-CNRS, BP 53, 38041 Grenoble Cedex 9, France.
[2] Present address: Seismological Laboratory, Mc Cone Hall, UC Berkeley, Berkeley CA 94720-4760, USA.

0021-9991/03/$ - see front matter
doi:10.1016/S0021-9991(03)00119-0

differential travel times of body waves, measurements of phase and group velocities of surface waves, and waveforms analysis have allowed global tomography to infer the heterogeneity distribution of seismic wave speeds, anisotropy and intrinsic attenuation within the Earth's interior [1–4]. Direct numerical simulation is now required: (i) to better understand the physics of wave propagation in spherical heterogeneous models; (ii) to assess the impact of the theoretical approximations, used in practice to compute synthetic seismograms, on the tomographic models; and (iii) to assess the resolution of the seismic records and tomographic models with respect to small scale heterogeneities.

Current methods used in global seismology are based upon spectral transform methods (STM) combined with perturbative expansions around a spherically symmetric reference configuration. On one hand, STM [5–8], which expand the solution and the physical variables into vector spherical harmonics, are remarkably accurate and they avoid the so-called pole problem. On the other hand, perturbation theories always assume small lateral variations in amplitude and small lateral gradients.

Among these methods, the use of normal modes summation has long been in the heart of global seismology [3]. The normal modes of a reference spherical configuration, which are used as intermediate functions for the computation of the seismograms, provide a complete basis in which aspherical and lateral perturbations are further expanded [9]. In the case of lateral variations, the most sophisticated normal modes methods [10–12] require to couple the modes along the same dispersion branch, while multiple scattering is taken into account in the limit of the order retained in the perturbation. Even when restricted to a second-order approximation, these methods face serious computational limits when dealing with dominant periods lower than 50 s, which are actually required for realistic modeling of surface waves (with periods as short as 25 s) or body waves (with typical periods of less than 10 s). For practical computations, high-frequency (asymptotic) approximations [13,14] are, therefore, retained, combined with Born approximations [15–18], generally limited to the first order. The high-frequency approximation is valid as long as the heterogeneities are much larger than the dominant propagating wavelength, while the first-order Born approximation assumes that they can be considered only as secondary sources.

Other STM bypass the intermediate step of calculating normal modes by solving directly the elastodynamic equation in the frequency domain, using either a strong [19] or a weak [20,21] formulation. In the latter case, the so-called direct solution method, a Galerkin approximation is performed, with the trial and weight functions being chosen as the tensor product of generalized spherical harmonics, combined with cubic splines or Chebychev polynomials in the radial direction. Again, when lateral variations are considered the coupling between modes results in a very large and often ill-conditioned algebraic system. Effective implementations of these methods then require some truncation in the actual coupling to be effectively solved.

STM involve the expansion of the variables, as well as the computation of spatial partial derivatives, into a non-local spherical harmonics basis. The major drawbacks are, therefore: (i) the need for high-order spherical expansions when lateral variations become rough and spatially localized; (ii) the use of a perturbative approximation when dealing with an aspherical geometry; (iii) the difficulty to incorporate mesh refinement; and (iv) the inherent computational complexity and communication overheads. The last issue is due to the fact that STM require a Legendre transformation in longitude, based on a non-uniform distribution of Gauss points [22].

All the methods previously mentioned solve the elastodynamic problem in the frequency domain and, therefore, do not directly provide informations on wave propagation within the model. A number of studies, using finite differences (FD) [23,24] or pseudo-spectral (PS) [25,26] methods have been recently conducted toward direct numerical simulation (DNS) of seismic wave propagation in spherical Earth models. Until now, they have been applied to rather restricted approximations, i.e., axisymmetric P and SV [26] or SH wave propagation [23,24], thus avoiding the inherent pole problem while reducing the computational requirements. The major problem in adapting these grid-based methods to arbitrary spherical geometry is that they do not provide a uniform representation of scalar functions on a sphere. Latitude–

longitude grids are indeed highly non-isotropic with a clustering of points near the poles that leads to severe CFL conditions. A possible way to circumvent the pole problem is the resort to a multidomain approach, a kind of computational divide et impera in which each domain inherits its own coordinate system [27–31]. However, in the context of FD methods, the main difficulty is to glue together the different coordinate systems. This requires the use of composite mesh methods [32] with overlapping regions between the meshes of each subdomain. The interpolation error and the size of the overlap regions lead to severe stability conditions.

Moreover, FD methods, widely used in exploration seismology, suffer from grid dispersion near strong gradients and require a large number of grid points per propagating wavelength in order to be accurate [33,34]. Balancing the trade-off between the numerical dispersion and the computational cost turns out to be difficult and often critical for global seismology studies. Higher order methods like PS methods allow for a non-dispersive propagation with only a few grid points per wavelength. A maximal efficiency is obtained when using Fast Fourier Transform but for more general boundary conditions the set of truncated Fourier series are often replaced by algebraic polynomials of Chebychev or Legendre type [35], with the drawback of introducing collocation points that are non-uniformly spaced. This last limitation can lead to stability problems even though it can be partly overcome with the help of generalized coordinates [36,37]. Finally, both FD and PS methods are based upon a strong formulation of the elastodynamic equation, and, therefore, face severe limitations for the approximation of free-surface boundary or interface continuity conditions. This makes these methods difficult to use in global seismology, as they fail to provide an accurate solution for surface or interface wave propagation.

New DNS methods must meet several requirements in order to be adapted to global seismology: (i) an accurate discretization of spherical and aspherical geometries; (ii) a natural approximation of surface boundary and interface continuity conditions; (iii) an expansion of the physical variables into basis of functions with local spatial support; (iv) an accurate conservation of energy and angular momentum for long time propagation; and (v) a minimal numerical dispersion on both body and surface waves with a small number of points per propagating wavelength.

The first steps toward the formulation and the parallel implementation of a new explicit spectral element method (SEM) that satisfies requirements (i)–(v) is considered in this paper. The principal motivation for adopting the SEM [38–40] is that it combines the geometrical flexibility of classical finite element methods with the exponential convergence rate associated with the spectral methods. Based upon a weak variational formulation of the elastodynamic equation, the SEM suffers from minimal numerical dispersion and allows for a natural treatment of boundary conditions. The SEM has been shown to be very efficient for elastic wave propagation problems within the context of regional seismology, and in particular to accurately model surface wave propagation [41–45]. The spatial discretization is based upon Legendre polynomials which, together with the use of a Gauss–Lobatto–Legendre quadrature, leads to a diagonal mass matrix and a fully explicit time scheme [44], while retaining the efficient sum-factorization techniques [46].

As in the finite element method, a special care is required to allow the SEM to deal with fluid regions. This can not be achieved by simply setting the shear modulus to zero since spurious oscillations are likely to appear as a consequence of the incorrect discretization of the kernel of the elastic operator [47]. Furthermore, the kinematic condition to be imposed at the fluid–solid boundaries would not be satisfied, since it only involves the normal component of the displacement. A first approach to solve the problem is to use a displacement formulation based upon lower order elements in the fluid, the coupling with the solid being satisfied in a weak sense [47]. Another possibility is to derive a scalar wave equation for the fluid and to force the continuity of traction and normal velocity at the fluid–solid interfaces. The fluid can be described either by a velocity potential if the density is constant [48,49] or by a momentum potential for a varying density [50]. Whenever self-gravitation is considered, an additional complication arises due to the presence of gravity modes and possible convective modes in the fluid. Because of the absence of observational evidence in the fluid outer core, these oscillations are routinely ignored when computing synthetic

seismograms in global seismology. It should be emphasized, however, that solving the equations in the general case is an open problem since the spectrum of the gravito-elastic operator is known to be continuous [51]. Note finally that whereas gravity and convective modes can be easily filtered out in the frequency domain (they are below the gravest elastic oscillation), there is no such way to proceed in the time domain. Our description will thus be restricted to the case of a neutrally stratified fluid.

In this paper we address the main extensions that are required for using the SEM in global seismology, and more generally for adapting it to spherical geometry. The results presented hereafter are based essentially upon the work of Chaljub [52], except for the fluid regions of the model for which we propose a discretization in terms of a velocity potential that generalizes the work presented by Komatitsch and Tromp [50] to the self-gravitating case. An alternative strategy to model the fluid regions can be found in [53], where the coupling of the SEM with a modal solution is presented. This approach is nevertheless restricted to spherical geometry, the sole case for which a semi-analytical solution can be derived.

The organization of the paper is as follows. A brief description of the elastodynamic equation that govern the wave propagation within a spherical, elastic, isotropic medium initially in a hydrostatic state of equilibrium under gravity loading, is outlined in Section 2. The effects of gravity are considered within the Cowling approximation [54] and the fluid is described in terms of the velocity potential. We refer to [50] and the references therein for the incorporation of additional effects such as anisotropy and attenuation. A hybrid variational formulation of the problem is then addressed in Section 3. The main motivation for adopting a hybrid approach is to ensure that non-conforming domain decomposition and mesh refinement, following the mortar element method [55,56], is a particular case of the general formulation. Such mesh refinement flexibility is crucial for an accurate representation of localized heterogeneities within a global model while reducing the computational cost in contrast to more conventional non-uniform meshes, like the one used in [50]. Matters of geometrical discretization, which is a key issue for extending the SEM to spherical geometry, are discussed in the first part of Section 4 in which a paving technique of a sphere using hexahedra is presented. All the transformations involved are defined analytically and, in contrast with FD methods, the SEM provides a natural setting for handling the connections between the different regions of the mesh. A spectral element discretization, associated with the hybrid variational formulation, is detailed in the remaining part of Section 4. Section 5 is dedicated to the formulation of an explicit predictor–corrector solver for the resulting discrete constrained algebraic system. It is shown that the computational cost induced by the non-conforming discretization becomes rapidly marginal as the size of the problem increases, which makes this formulation effective for the resolution of global scale wave propagation in heterogeneous spherical models. In Section 6, we confine our attention to the parallel implementation and the scalability of the method with respect to distributed memory architectures. Finally, selected numerical applications are developed in Section 7 which demonstrate the performance and the potentialities of the method.

2. Equations of motion

In this section we recall the equations of elastic wave propagation in a spherically symmetric, non-rotating, elastic, and isotropic medium. The equations are obtained by a first-order adiabatic perturbation around a reference state of hydrostatic equilibrium, and the effects of gravity are accounted for within the Cowling approximation. The physical meaning of this approximation is to consider that the mass fluctuation caused by seismic waves remains localized, and, therefore, does not affect the gravitational field. Whenever this assumption breaks down, the effects of self-gravitation must be accounted for and the perturbation of the gravitational potential must be considered. Note that since this potential is defined over the whole space $\mathbb{R}^3$, the issue of solving the equations of motion in an unbounded domain has then to be considered.

First we start with a description of the geometry and fix some notations that will be used throughout the paper. In the reference configuration, we consider a sphere which is identified to the open subset Ω, its surface is labeled $\partial\Omega$ and $\bar{\Omega}$ denotes the closed subset $\Omega \cup \partial\Omega$. The sphere is made of solid and fluid regions, which we, respectively, refer to as Ω^{S} and Ω^{F}:

$$\bar{\Omega} = \bar{\Omega}^{\mathrm{S}} \cup \bar{\Omega}^{\mathrm{F}}. \tag{1}$$

Each region is further decomposed into a set of non-overlapping open subdomains:

$$\begin{array}{ll} \bar{\Omega}^{\mathrm{S}} = \bigcup_{\kappa=1}^{K} \bar{\Omega}_{\kappa}^{\mathrm{S}} & \forall \kappa, \kappa' \in \{1 \ldots K\} \;\; \Omega_{\kappa}^{\mathrm{S}} \cap \Omega_{\kappa'}^{\mathrm{S}} = \emptyset, \\ \bar{\Omega}^{\mathrm{F}} = \bigcup_{l=1}^{\underline{L}} \bar{\Omega}_{l}^{\mathrm{F}} & \forall l, l' \in \{1 \ldots L\} \;\; \Omega_{l}^{\mathrm{F}} \cap \Omega_{l'}^{\mathrm{F}} = \emptyset. \end{array} \tag{2}$$

Whenever two solid subdomains $\Omega_{\kappa}^{\mathrm{S}}$ and $\Omega_{\kappa'}^{\mathrm{S}}$ are in contact, $\Gamma_{\underline{\kappa}} = \bar{\Omega}_{\kappa}^{\mathrm{S}} \cap \bar{\Omega}_{\kappa'}^{\mathrm{S}}$ stands for their common interface. Similarly, $\Gamma_{\underline{l}}$ denotes the boundary between the two neighboring fluid subdomains Ω_{l}^{F} and $\Omega_{l'}^{\mathrm{F}}$. We refer to Σ_{SS} as the union of the $\underline{K}$ internal solid–solid boundaries, to Σ_{FF} as the collection of the $\underline{L}$ fluid–fluid boundaries, and Σ_{SF} stands for the set of solid–fluid boundaries. The union of all interfaces, including the outer surface, is labeled Σ and is such that: $\Sigma = \Sigma_{\mathrm{SS}} \cup \Sigma_{\mathrm{FF}} \cup \Sigma_{\mathrm{SF}} \cup \partial\Omega$. For the sake of simplicity we only consider the case where all the interfaces are spherical, so that each subdomain is either a sphere or a spherical shell.

2.1. Solid regions

Under those assumptions, solving the problem of elastic waves propagation consists in finding the displacement vector field $\mathbf{u}(\mathbf{x}, t)$ for $\mathbf{x} \in \Omega^{\mathrm{S}}$ and $t \in [0, T]$ such that (see, for example [3, p. 102]):

$$\rho\ddot{\mathbf{u}} - \nabla \cdot \mathbf{T}(\mathbf{u}) + \{\nabla \cdot (\rho\mathbf{u})\}\mathbf{g} - \nabla(\rho\mathbf{u} \cdot \mathbf{g}) = \mathbf{f}, \tag{3}$$

where $\mathbf{T}(\mathbf{u})$ is the Lagrangian incremental stress tensor, ρ is the mass density, $\mathbf{g}$ is the acceleration due to gravity and $\mathbf{f}$ is a generalized body force. In Eq. (3) a dot over a symbol implies time derivation, while $\nabla\boldsymbol{\tau}$ and $\nabla \cdot \boldsymbol{\tau}$, respectively, denote the gradient and the divergence of a given tensor field $\boldsymbol{\tau}$.

The incremental stress tensor $\mathbf{T}(\mathbf{u})$ is linearly related to the infinitesimal strain tensor $\boldsymbol{\varepsilon}(\mathbf{u}) = \frac{1}{2}(\nabla\mathbf{u} + \nabla^{t}\mathbf{u})$ through Hooke's law:

$$\mathbf{T}_{ij}(\mathbf{u})(\mathbf{x}, t) = \boldsymbol{\Upsilon}_{ijkl}(\mathbf{x})\boldsymbol{\varepsilon}_{kl}(\mathbf{u})(\mathbf{x}, t) \quad \forall \mathbf{x} \in \Omega^{\mathrm{S}}, \; \forall t \in [0, T], \tag{4}$$

where the fourth-order tensor $\boldsymbol{\Upsilon}$ controls the velocity of propagating waves in the medium. Then, because the pre-stress is hydrostatic, $\boldsymbol{\Upsilon}$ possesses the classical symmetries:

$$\boldsymbol{\Upsilon}_{ijkl} = \boldsymbol{\Upsilon}_{ijlk} = \boldsymbol{\Upsilon}_{jikl} = \boldsymbol{\Upsilon}_{klij}. \tag{5}$$

Furthermore, if we assume an isotropic body then $\boldsymbol{\Upsilon}$ can be fully represented by its two Lamé's parameters λ and μ:

$$\boldsymbol{\Upsilon}_{ijkl} = \lambda\boldsymbol{\delta}_{ij} + \mu(\boldsymbol{\delta}_{ik}\boldsymbol{\delta}_{jl} + \boldsymbol{\delta}_{il}\boldsymbol{\delta}_{jk}), \tag{6}$$

where $\boldsymbol{\delta}$ is the Kronecker delta.

2.2. Fluid regions

We consider an inviscid fluid which is initially in a state of hydrostatic equilibrium. Let ρ and p, respectively, stand for the mass density and the pressure of the fluid in this reference configuration, with the density being continuous throughout the fluid. We refer to the Eulerian adiabatic perturbations of ρ and p as ρ' and p', the latter being related to the Lagrangian perturbations of pressure δp and density $\delta\rho$ via:

$$\delta p = p' + \rho \mathbf{u} \cdot \mathbf{g}, \tag{7}$$

$$\delta \rho = \rho' + \mathbf{u} \cdot \nabla \rho, \tag{8}$$

where $\mathbf{u}$ is the displacement perturbation and $\mathbf{g}$ is the acceleration of gravity. The Lagrangian perturbations of pressure and density are related by:

$$\delta \rho = \frac{1}{c^2} \delta p, \tag{9}$$

where c is the sound speed in the fluid. The equivalent relation between the Eulerian perturbations writes:

$$\rho' = \frac{1}{c^2} p' - \mathbf{u} \cdot \mathbf{s}, \tag{10}$$

where $\mathbf{s}$ is the "stratification", or Schwarzschild vector, that characterizes the behavior of the fluid to changes in density:

$$\mathbf{s} = \nabla \rho - \frac{\rho}{c^2} \mathbf{g}. \tag{11}$$

It is more common to describe the stratification of the fluid through the so-called Brunt–Väisälä or buoyancy frequency N:

$$N^2 = \frac{1}{\rho} \mathbf{s} \cdot \mathbf{g}. \tag{12}$$

Whenever N (or $||\mathbf{s}||$) is non-zero, buoyancy acts as an additional restoring force that causes gravity or convective oscillations to occur in the fluid. As discussed previously, we restrict our study to the case of a neutrally stratified fluid, that is to $N = 0$. This implies that the gravity vector must satisfy:

$$\mathbf{g} = \frac{c^2}{\rho} \nabla \rho, \tag{13}$$

and that Eq. (10) takes the form:

$$\rho' = \frac{1}{c^2} p'. \tag{14}$$

To derive the wave equation, we start with the first-order accurate continuity equation [57,58]:

$$\dot{\rho}' + \nabla \cdot (\rho \mathbf{v}) = 0, \tag{15}$$

where $\mathbf{v}$ is the velocity field in the fluid. Then, neglecting mass redistribution as well as any source term in the fluid, the conservation of momentum writes:

$$\rho \dot{\mathbf{v}} = -\nabla p' + \rho' \mathbf{g}. \tag{16}$$

Taking the value of $\mathbf{g}$ and ρ', respectively, from (13) and (14), we obtain:

$$\dot{\mathbf{v}} = -\nabla \left(\frac{1}{\rho} p' \right). \tag{17}$$

This last equation ensures that the velocity field $\mathbf{v}$ remains irrotational with time, consistent with the assumption that convection is neglected. We then introduce the velocity potential Φ which is defined as:

$$\mathbf{v} = -\nabla \Phi. \tag{18}$$

Considering the momentum Eq. (17) and the assumption that the fluid is initially at rest, yields the following relation between the velocity potential and the Eulerian pressure perturbation:

$$p' = \rho\dot{\mathbf{\Phi}}. \tag{19}$$

Finally, plugging (18) and (19) into (15) and using (14) yields the scalar wave equation for the velocity potential:

$$\frac{1}{c^2}\ddot{\mathbf{\Phi}} = \frac{1}{\rho}\nabla\cdot\{\rho\nabla\Phi\}. \tag{20}$$

2.3. Initial and boundary conditions

The equations of motion (3) and (20) have to be completed with both initial and boundary conditions. The initial conditions are set consistently with the assumption that the medium is at rest in the reference configuration:

$$\mathbf{u}(\mathbf{x},0) = \dot{\mathbf{u}}(\mathbf{x},0) = \mathbf{0} \quad \forall\mathbf{x}\in\Omega^{\mathrm{S}}, \tag{21}$$

$$\Phi(\mathbf{x},0) = \dot{\Phi}(\mathbf{x},0) = 0 \quad \forall\mathbf{x}\in\Omega^{\mathrm{F}}. \tag{22}$$

We must then specify the kinematic and dynamic conditions that hold on the different interfaces of the medium. First, recall that for the solid subdomains to remain in welded contact, the displacement vector must be continuous across internal solid–solid boundaries:

$$[|\,\mathbf{u}(\mathbf{x},t)\,|]_{\Sigma_{\mathrm{SS}}} = \mathbf{0} \quad \forall\mathbf{x}\in\Sigma_{\mathrm{SS}},\ \forall t\in[0,T], \tag{23}$$

where $[|\ \ |]_{\Gamma}$ stands for the jump operator across the oriented surface Γ.

Then, because tangential slip is allowed on every interface where a fluid is involved, only the normal component of the velocity vector has to be continuous there:

$$[|\,\mathbf{v}(\mathbf{x},t)\,|]_{\Sigma_{\mathrm{SF}}\cup\Sigma_{\mathrm{FF}}}\cdot\mathbf{n}(\mathbf{x}) = 0 \quad \forall\mathbf{x}\in\Sigma_{\mathrm{SF}}\cup\Sigma_{\mathrm{FF}},\ \forall t\in[0,T], \tag{24}$$

with $\mathbf{n}$ being the unit normal to the interface. Note that the normal displacement is also continuous as a consequence of the initial condition (21).

Finally, the traction vector must be continuous across every interface, according to the action–reaction principle. On the internal boundaries between solid subdomains, this reads:

$$[|\,\mathbf{T}(\mathbf{u})(\mathbf{x},t)\cdot\mathbf{n}(\mathbf{x})\,|]_{\Sigma_{\mathrm{SS}}} = \mathbf{0} \quad \forall\mathbf{x}\in\Sigma_{\mathrm{SS}},\ \forall t\in[0,T], \tag{25}$$

where $\mathbf{n}$ stands for the unit normal to any interface in Σ_{SS}. For the solid–fluid boundaries, the continuity of traction takes the form:

$$\mathbf{T}(\mathbf{u})(\mathbf{x},t)\cdot\mathbf{n}(\mathbf{x}) = -\delta p\,\mathbf{n}(\mathbf{x}) \quad \forall\mathbf{x}\in\Sigma_{\mathrm{SF}},\ \forall t\in[0,T], \tag{26}$$

where δp is defined by (7) and $\mathbf{n}$ stands for the unit vector normal to the interface and pointing outward the solid region. Eq. (26) tells that the deviatoric (shear) stress in the solid must vanish when approaching the solid–fluid interfaces, since the fluid is assumed to be inviscid. On the fluid–fluid boundaries, the counterpart of (25) is:

$$[|\,\delta p(\mathbf{x},t)\,|]_{\Sigma_{\mathrm{FF}}} = 0 \quad \forall\mathbf{x}\in\Sigma_{\mathrm{FF}},\ \forall t\in[0,T]. \tag{27}$$

From the definition of both δp (7) and Φ (19), and since the density, the gravity and the normal displacement are continuous throughout the fluid, this is also equivalent to:

$$[|\dot{\mathbf{\Phi}}(\mathbf{x},t)|]_{\Sigma_{\mathrm{FF}}} = 0 \quad \forall \mathbf{x} \in \Sigma_{\mathrm{FF}},\ \forall t \in [0,T]. \tag{28}$$

Eventually, as we neglect the action of the region exterior to Ω, the surface of the sphere acts as a free boundary. Assuming that the free surface is on top of a solid region, the following conditions applies:

$$\mathbf{T}(\mathbf{u})(\mathbf{x},t)\cdot\mathbf{n}(\mathbf{x}) = \mathbf{0} \quad \forall \mathbf{x} \in \partial\Omega \cap \bar{\Omega}^{\mathrm{S}},\ \forall t \in [0,T]. \tag{29}$$

3. Hybrid variational formulation

In this section we present a variational formulation in space of the equations of motion (3) and (20), where the continuity of both the displacement between solid subdomains and the velocity potential between fluid subdomains is expressed in a weak sense. This framework will be further used when adapting the SEM to deal with non-conforming interfaces, as those introduced during the meshing process. The matching between solid and fluid regions is imposed in a strong form and relies on the explicit forcing of the continuity of traction and normal velocity.

Let $H^1(\mathscr{O})$ denote the space of scalar fields which, together with their first derivatives, are square integrable on the open set $\mathscr{O}$, and let $\mathbf{H}^1(\mathscr{O})$ stand for the space of vector fields which components are in $H^1(\mathscr{O})$. The space of admissible displacements $\mathscr{V}^{\mathrm{S}}$ is defined in the solid regions as the product of these local spaces:

$$\mathscr{V}^{\mathrm{S}} = \prod_{\kappa=1}^{K} \mathbf{H}^1(\Omega_\kappa^{\mathrm{S}}). \tag{30}$$

Note that the continuity between subdomains is not enforced in the definition of $\mathscr{V}^{\mathrm{S}}$. Let indeed $\Gamma_{\underline{\kappa}}$ be an inner solid–solid boundary and $\mathbf{v}$ be an admissible displacement field, then $\mathbf{v}$ can be defined on $\Gamma_{\underline{\kappa}}$ as the trace of either $\mathbf{v}_{|_{\Omega_\kappa^{\mathrm{S}}}}$ or $\mathbf{v}_{|_{\Omega_{\kappa'}^{\mathrm{S}}}}$, where $\mathbf{v}_{|_{\Omega_\kappa^{\mathrm{S}}}}$ (resp. $\mathbf{v}_{|_{\Omega_{\kappa'}^{\mathrm{S}}}}$) stands for the restriction of $\mathbf{v}$ to $\Omega_\kappa^{\mathrm{S}}$ (resp. $\Omega_{\kappa'}^{\mathrm{S}}$). We rather consider the continuity conditions for the displacements as additional constraints, which are expressed through the introduction of a set of Lagrange multipliers. The multipliers span the dual space of displacements on the solid–solid interfaces:

$$\mathscr{M}^{\mathrm{S}} \subset \prod_{\underline{\kappa}=1}^{\underline{K}} \mathbf{H}^{-(1/2)}(\Gamma_{\underline{\kappa}}). \tag{31}$$

In the fluid regions, we similarly define the space of admissible potentials as:

$$\mathscr{V}^{\mathrm{F}} = \prod_{l=1}^{L} H^1(\Omega_l^{\mathrm{F}}), \tag{32}$$

and we introduce another set of Lagrange multipliers to account for the continuity of the velocity potentials throughout the fluid:

$$\mathscr{M}^{\mathrm{F}} \subset \prod_{\underline{l}=1}^{\underline{L}} H^{-(1/2)}(\Gamma_{\underline{l}}). \tag{33}$$

The weak form associated to the gravito-elastodynamic equations can be set under a primal hybrid formulation [59] which consists, $\forall t \in [0,T]$, in finding $(\mathbf{u}_t, \boldsymbol{\lambda}_t^{\mathrm{S}}) \in \mathscr{V}^{\mathrm{S}} \times \mathscr{M}^{\mathrm{S}}$ in the solid regions, and $(\Phi_t, \lambda_t^{\mathrm{F}}) \in \mathscr{V}^{\mathrm{F}} \times \mathscr{M}^{\mathrm{F}}$ in the fluid regions such that:

$$\forall(\mathbf{v},\boldsymbol{\mu}^{\mathrm{S}})\in\mathscr{V}^{\mathrm{S}}\times\mathscr{M}^{\mathrm{S}}\text{ and }\forall(\Psi,\mu^{\mathrm{F}})\in\mathscr{V}^{\mathrm{F}}\times\mathscr{M}^{\mathrm{F}}:\tag{34}$$

$$\left(\rho\ddot{\mathbf{u}}_t,\mathbf{v}\right)_{\Omega^{\mathrm{S}}}+\mathscr{A}^{\mathrm{S}}(\mathbf{u}_t,\mathbf{v})+\mathscr{C}^{\mathrm{S}}(\dot{\Phi}_t,\mathbf{v})+\mathscr{B}^{\mathrm{S}}(\mathbf{v},\boldsymbol{\lambda}^{\mathrm{S}}_t)=(\mathbf{f},\mathbf{v})_{\Omega^{\mathrm{S}}},\tag{35}$$

$$\mathscr{B}^{\mathrm{S}}(\mathbf{u}_t,\boldsymbol{\mu}^{\mathrm{S}})=0,\tag{36}$$

$$\left(\frac{\rho}{c^2}\ddot{\Phi}_t,\Psi\right)_{\Omega^{\mathrm{F}}}+\mathscr{A}^{\mathrm{F}}(\Phi_t,\Psi)+\mathscr{C}^{\mathrm{F}}(\dot{\mathbf{u}}_t,\Psi)+\mathscr{B}^{\mathrm{F}}(\Psi,\lambda^{\mathrm{F}}_t)=0,\tag{37}$$

$$\mathscr{B}^{\mathrm{F}}(\dot{\Phi}_t,\mu^{\mathrm{F}})=0,\tag{38}$$

with the initial conditions:

$$(\mathbf{u}_0,\mathbf{v})_{\Omega^{\mathrm{S}}}=(\dot{\mathbf{u}}_0,\mathbf{v})_{\Omega^{\mathrm{S}}}=0,\tag{39}$$

and

$$(\Phi_0,\Psi)_{\Omega^{\mathrm{F}}}=(\dot{\Phi}_0,\Psi)_{\Omega^{\mathrm{F}}}=0.\tag{40}$$

In the previous equations, $(\cdot,\cdot)_{\Omega^{\mathrm{S}}}$ and $(\cdot,\cdot)_{\Omega^{\mathrm{F}}}$, respectively, denote the L^2 scalar products in Ω^{S} and Ω^{F}, and $\mathbf{v}_t$ stands for the snapshot at time t of any given space-and-time vector field $\mathbf{v}$.

$\mathscr{A}^{\mathrm{S}}$ is the bilinear form related to the gravito-elastic operator in the solid regions. It is obtained by dotting the three last terms on the left-hand side of Eq. (3) by an admissible displacement $\mathbf{v}$, then integrating by parts to retain the volume term. It can be written as [60]:

$$\mathscr{A}^{\mathrm{S}}(\mathbf{u},\mathbf{v})=\int_{\Omega^{\mathrm{S}}}\boldsymbol{\varepsilon}(\mathbf{u}):\boldsymbol{\Upsilon}:\boldsymbol{\varepsilon}(\mathbf{v})\,\mathrm{d}\Omega+\int_{\Omega^{\mathrm{S}}}\rho\mathrm{Sym}\{(\mathbf{v}\cdot\mathbf{g})\nabla\cdot\mathbf{u}-\mathbf{u}\cdot\nabla(\mathbf{v}\cdot\mathbf{g})\}\,\mathrm{d}\Omega,\tag{41}$$

where the colon indicates a double tensorial contraction and $\mathrm{Sym}\{f(\mathbf{u},\mathbf{v})\}=\frac{1}{2}(f(\mathbf{u},\mathbf{v})+f(\mathbf{v},\mathbf{u}))$. The first integral in (41) is related to the elastic response of the medium while the second term accounts for gravity. After integrating by parts, an additional surface term arises which involves the traction at both the free surface and the fluid–solid boundaries. The former is set to zero, consistently with the free traction condition (29), while in the latter the normal traction in the solid is replaced by the pressure of the fluid side, according to (26). This substitution yields the coupling operator $\mathscr{C}^{\mathrm{S}}$:

$$\mathscr{C}^{\mathrm{S}}(\dot{\Phi},\mathbf{v})=\int_{\Sigma_{\mathrm{SF}}}\rho_{\mathrm{F}}\left(\dot{\Phi}+\mathbf{u}\cdot\mathbf{g}\right)\mathbf{v}\cdot\mathbf{n}\,\mathrm{d}\Gamma,\tag{42}$$

where ρ_{F} is the density of the fluid side and $\mathbf{n}$ is the unit normal to the interface which points outward of the solid region.

Finally, the bilinear form $\mathscr{B}^{\mathrm{S}}$ combines the jumps of displacement together with the tractions on the boundaries between subdomains:

$$\mathscr{B}^{\mathrm{S}}(\mathbf{u},\boldsymbol{\mu}^{\mathrm{S}})=\sum_{\underline{\kappa}=1}^{\underline{K}}\int_{\Gamma_{\underline{\kappa}}}(\mathbf{u}_{\kappa}-\mathbf{u}_{\kappa'})\cdot\boldsymbol{\mu}^{\mathrm{S}}_{\underline{\kappa}}\,\mathrm{d}\Gamma,\tag{43}$$

where $\mathbf{u}_{\kappa}$ and $\mathbf{u}_{\kappa'}$ denote the traces of $\mathbf{u}_{|\Omega^{\mathrm{S}}_{\kappa}}$ and $\mathbf{u}_{|\Omega^{\mathrm{S}}_{\kappa'}}$ over $\Gamma_{\underline{\kappa}}$. The definition of $\mathscr{B}^{\mathrm{S}}$ makes it clear that Eq. (36) expresses the continuity of displacement across each interface $\Gamma_{\underline{\kappa}}$ in a weak sense, i.e., according to the duality between $\mathbf{H}^{1/2}(\Gamma_{\underline{\kappa}})$ and $\mathbf{H}^{-(1/2)}(\Gamma_{\underline{\kappa}})$. Note that the displacement field obtained by solving Eqs. (35)

and (36) is globally continuous, that is $\mathbf{u}_t \in \mathbf{H}^1(\Omega^S)$. Furthermore, the Lagrange multiplier $\boldsymbol{\lambda}_t^S$ is nothing but the related traction on the solid–solid interfaces: $\boldsymbol{\lambda}_t^S(\mathbf{x}) = \mathbf{T}(\mathbf{u}_t) \cdot \mathbf{n}(\mathbf{x}) \ \forall \mathbf{x} \in \Sigma_{SS}$.

In the fluid regions, dotting the right-hand side of the scalar wave equation (20) and integrating by parts yields a volume term, from which we define the bilinear form $\mathscr{A}^F$:

$$\mathscr{A}^F(\Phi, \Psi) = \int_{\Omega^F} \rho \nabla \Phi \cdot \nabla \Psi \, d\Omega, \tag{44}$$

and a surface integral in which the normal derivative of the velocity potential is replaced by the normal velocity of the solid side to account for (24):

$$\mathscr{C}^F(\dot{\mathbf{u}}, \Psi) = \int_{\Sigma_{SF}} \rho_F \dot{\mathbf{u}} \cdot \mathbf{n} \Psi \, d\Gamma, \tag{45}$$

with $\mathbf{n}$ being the unit normal to the interface which points outward of the fluid.

Lastly, the bilinear form $\mathscr{B}^F$ combines the two dual variables Φ and μ^F on the fluid–fluid interfaces:

$$\mathscr{B}^F(\Phi, \mu^F) = \sum_{\underline{l}=1}^{\underline{L}} \int_{\Gamma_{\underline{l}}} (\Phi_l - \Phi_{l'}) \mu_{\underline{l}}^F \, d\Gamma. \tag{46}$$

Note again that the continuity of the velocity potential across the fluid subdomains is expressed in a weak sense by (38). Furthermore, solving Eqs. (37) and (38) yields a globally continuous potential Φ_t and a Lagrange multiplier μ^F, which appears as the normal momentum on the boundaries between the fluid subdomains: $\mu_t^F(\mathbf{x}) = \rho \nabla \Phi_t \cdot \mathbf{n}(\mathbf{x}) \ \forall \mathbf{x} \in \Sigma_{SF}$.

4. Spectral element approximation

This section deals with a spectral element approximation to elastic wave propagation in spherical geometry. The method is based upon a Galerkin approximation of Eqs. (35)–(38), which is built by following a three-steps procedure. First a geometrical discretization is performed, which consists in paving the sphere into hexahedral elements. Second a functional discretization for the spaces of admissible displacements, potentials and Lagrange multipliers is provided, which naturally relies on the sphere decomposition. Third a numerical approximation is applied to evaluate the integrals present in the variational formulation. Once completed, the spatial approximation yields a system of ordinary differential equations in time, which is eventually solved by a finite difference scheme.

4.1. Geometrical discretization

The building of a mesh is a classical issue for any numerical method dealing with spherical geometry. Many efforts have consequently been devoted to this subject for the study of global processes such as atmospheric and oceanic circulation, or convection in the Earth's mantle and outer core. However, contrary to these examples in which the space domain is either a 2-sphere or a 3D spherical shell, modeling seismic wave propagation requires to tile an entire sphere.

The use of the classical SEM puts the additional constraint that the spherical grid must be built with hexahedra. Furthermore, two requirements should be fulfilled by the final mesh. First, all the spherical interfaces of the model should be explicitly discretized, henceforth allowing for abrupt radial variations of the elastic parameters to be considered. Second, the spherical mapping should be as regular as possible in the sense that the elements of the mesh are not too distorted and the grid-points sampling is uniform.

To satisfy the first constraint, we must be able to tile a 2-sphere with quadrangles. A classical approach for defining such a mesh is to use the central (also called gnomic) projection of a cube onto its circumscribed sphere. Such a mapping, known as the "cubed sphere" transformation or the "cubic-gnomic" projection, has been introduced by Sadourny [27] and used by Ronchi et al. [31] to define a finite difference approximation of partial differential equations in spherical geometry. It has also been used in a spectral element approach of the shallow water equations on the 2-sphere [61].

Through the cubed sphere transformation, the sphere is decomposed into six regions which are isomorphic to the six faces of a cube. A spherical grid can further be obtained by projecting a quadrangular mesh of the surface of the cube back to the sphere. Fig. 1 shows the result of transporting a 16×16 structured mesh from one face of the cube onto the sphere. As a consequence of the gnomic projection, any straight line drawn on a face of the cube is transformed into a geodesic on the sphere. The 2D paving obtained on the sphere has the desired property of being quite uniform, since the deformation rate among each of its faces does not exceed 30%.

The process of building a hexahedral spherical mesh is depicted in Fig. 2. First, from the discretization of the 2-sphere it is straightforward to build a 3D mesh inside a spherical shell, by radially connecting the quadrangles between two concentric cubed spheres. Once each spherical boundary has been provided with its own discretization, we introduce a progressive transition from the deepest interface to a uniform cube that lies at the center of the mesh. The analytic expression for this transformation is given in Appendix A.

The 3D mesh obtained from the construction described so far suffers from a non-uniform grid-points sampling with depth. This drawback, which is intrinsic to the process of connecting concentric spheres, causes the lateral size of each element to decrease proportionally to the radius. As a consequence, the sampling of the wavelengths, which is the critical ratio with regard to the accuracy of the method, is also an increasing function of depth. Note that this effect will be even more pronounced when seismic velocities increase with depth, as they do in planetary interiors. We want to circumvent such a non-uniform property for two reasons. First, the presence of over-sampled regions in the model would imply unnecessary calculations and memory storage. Second, any conditionally stable scheme used for time marching would be penalized by the smallest distance between grid-points when imposing the time step to satisfy the CFL condition. To overcome this difficulty, we allow for a possible coarsening of the grid at a given depth. By doing so, we implicitly break the property of "geometrical conformity" following which two neighboring elements have to share an entire edge, or an entire face. The resulting 3D mesh is said to be geometrically non-conforming, and we hereafter refer to the boundaries between non-matching grids as the "non-conforming interfaces".

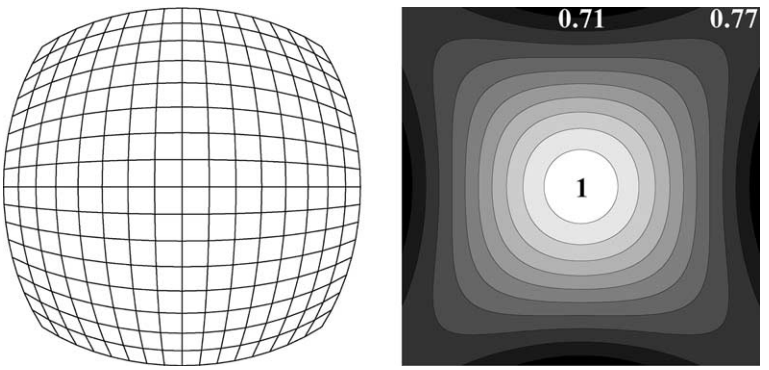

Fig. 1. One face of the "cubed sphere" is shown on the left. It is obtained by a gnomic projection of a 16×16 quadrangular grid from one face of a reference cube to its circumscribed sphere. Contour lines of the surface area density within the grid is shown on the right plot. Exact values range from 0.71 on the border to 1 at the center of the face.

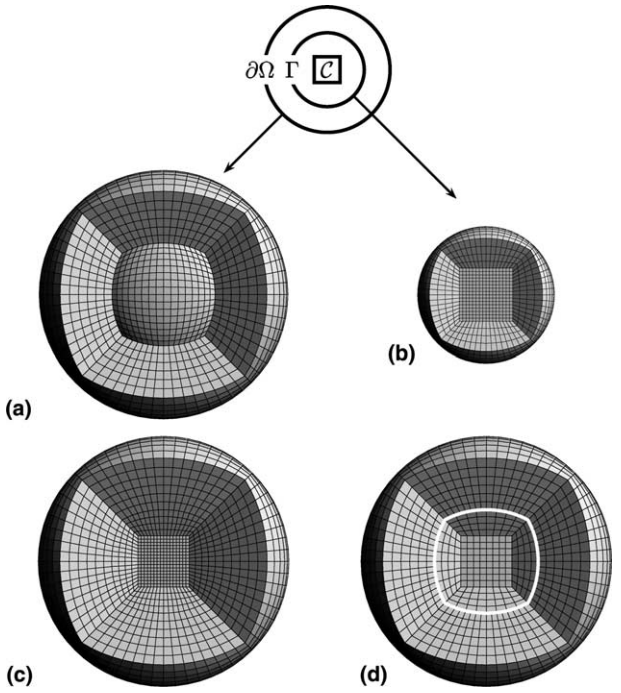

Fig. 2. Building of a 3D SEM mesh inside a sphere with a given spherical inner boundary Γ. Both Γ and the surface of the sphere $\partial\Omega$ are discretized via the cubed sphere transformation, then radially connected to fill the 3D spherical shell (a). A transition from Γ to a central cube $\mathscr{C}$ is then performed to fill the inner part of the mesh (b). The 3D spherical grid obtained by adding (a) and (b) is shown in (c). To avoid the clustering of grid-points with depth, the central region is discretized with a twice coarser grid (d). The interface Γ which is displayed as a bold white line is said to be non-conforming. In each of the 3D plots, a cubic block is removed to permit a view into the volume.

4.2. Functional discretization

Following the paving strategy explained above, each solid subdomain $\Omega_\kappa^{\mathrm{S}}$ is decomposed into a set, which we denote $\boldsymbol{\tau}_\kappa$, of n_κ hexahedral elements:

$$\boldsymbol{\tau}_\kappa = \left(\tau_\kappa^e\right)_{e=1,n_\kappa}, \quad \bar{\Omega}_\kappa^{\mathrm{S}} = \bigcup_{e=1}^{n_\kappa} \bar{\tau}_\kappa^e. \tag{47}$$

The hexahedra are obtained from a reference unit cube, by an invertible local mapping: $\tau_\kappa^e = \mathscr{F}_\kappa^e(\Lambda^3)$, where $\Lambda = [-1,1]$. Note that the different mappings must be compatible in order to preserve the geometrical conformity within the subdomains. The displacements are then approximated by continuous fields on each solid subdomain, which are defined by transporting tensorized polynomials from the reference unit cube onto the elements of the mesh:

$$\mathscr{V}_{\mathrm{h}}^{\mathrm{S}} = \left\{ \mathbf{v}_{\mathrm{h}} \in \prod_{\kappa=1}^{K} \left(\mathscr{C}^0(\Omega_\kappa)\right)^3;\ \mathbf{v}_{\mathrm{h}}|\tau_\kappa^e \circ \mathscr{F}_\kappa^e \in \left(\mathbb{P}_N(\Lambda^3)\right)^3,\ \forall e = 1, \ldots, n_\kappa \right\}. \tag{48}$$

In the last expression, $\mathbf{v}_{\mathrm{h}}|\tau_\kappa^e$ is the restriction of $\mathbf{v}_{\mathrm{h}}$ to τ_κ^e, "$\circ$" denotes the functional composition and $\mathbb{P}_N$ stands for the set of polynomials of degree less or equal to N over each direction of space.

The approximated space for the velocity potentials in the fluid is defined in the same way:

$$\mathscr{V}_{\mathrm{h}}^{\mathrm{F}} = \left\{ \Psi_{\mathrm{h}} \in \prod_{l=1}^{L} \mathscr{C}^0(\Omega_l);\ \Psi_{\mathrm{h}}|\tau_l^e \circ \mathscr{F}_l^e \in \mathbb{P}_N(\Lambda^3),\ \forall e = 1, \ldots, n_l \right\}, \tag{49}$$

with τ_l^e standing for the hexahedral elements paving the fluid subdomains.

Similarly, the Lagrange multipliers are approximated by piece-wise polynomials based upon the 2D tiling of the non-conforming spherical interfaces. To fix the notations, recall that after the meshing process, every non-conforming solid–solid interface $\Gamma_{\underline{\kappa}} \in \Sigma_{\mathrm{SS}}$ inherits two quadrangulations from τ_κ and $\tau_{\kappa'}$. Let for example $\tau_{\underline{\kappa}}$ stand for either τ_κ or $\tau_{\kappa'}$, then $\tau_{\underline{\kappa}}$ provides $\Gamma_{\underline{\kappa}}$ with a quadrangulation that we shall denote $\upsilon_{\underline{\kappa}}$. Each of the $n_{\underline{\kappa}}$ quadrangles in $\upsilon_{\underline{\kappa}}$ is obtained from a reference unit square through an invertible 2D mapping: $\upsilon_{\underline{\kappa}}^e = \mathscr{G}_{\underline{\kappa}}^e(\Lambda^2)$. In this paper we have chosen $\tau_{\underline{\kappa}}$ to be the finer grid between τ_κ and $\tau_{\kappa'}$, although this is not a restriction imposed by the mortar element method.

A special care must then be taken to define the discrete space for the Lagrange multipliers. The polynomial order used in the approximation indeed determines the well-posedness of the saddle-point problem arising from the discretization, through the satisfaction of the so called LBB condition. Classical numerical analysis dedicated to non-matching grids in the finite element framework, like the FETI method [62] or the mortar element method [55,56,63], suggest that the polynomial degree of the dual variables (the multipliers) should be decreased compared to that used for the primal variables (the displacements in the solid or the velocity potentials in the fluid) in order to satisfy the LBB criterion. However, in the particular case where the non-conforming interfaces are spherical (or more generally closed), an equal-order interpolation yields a well-posed approximation. We thus define the discrete space of multipliers as:

$$\mathscr{M}_{\mathrm{h}}^{\mathrm{S}} = \left\{ \boldsymbol{\mu}_{\mathrm{h}}^{\mathrm{S}} \in \prod_{\underline{\kappa}=1}^{K} \left(\mathscr{C}^0(\Gamma_{\underline{\kappa}})\right)^3;\ \boldsymbol{\mu}_{\mathrm{h}}^{\mathrm{S}}|\upsilon_{\underline{\kappa}}^e \circ \mathscr{G}_{\underline{\kappa}}^e \in \left(\mathbb{P}_N(\Lambda^2)\right)^3,\ \forall e = 1, \ldots, n_{\underline{\kappa}} \right\}, \tag{50}$$

and

$$\mathscr{M}_{\mathrm{h}}^{\mathrm{F}} = \left\{ \mu_{\mathrm{h}}^{\mathrm{F}} \in \prod_{\underline{l}=1}^{L} \mathscr{C}^0(\Gamma_{\underline{l}});\ \mu_{\mathrm{h}}^{\mathrm{F}}|\upsilon_{\underline{l}}^e \circ \mathscr{G}_{\underline{l}}^e \in \mathbb{P}_N(\Lambda^2),\ \forall e = 1, \ldots, n_{\underline{l}} \right\}. \tag{51}$$

Now, for the discrete spaces to be explicitly constructed, the sets $\mathbb{P}_N(\Lambda^3)$ and $\mathbb{P}_N(\Lambda^2)$ must be provided with polynomial basis. We start by introducing the so-called Gauss–Lobatto–Legendre (hereafter denoted GLL) points, which are defined on the unit interval Λ as the zeroes of $(1-x^2)L'_N(x)$, where $L_N(x)$ is the Legendre polynomial of degree N. Note that the GLL points include the extremities of the unit segment Λ, which is a desirable property regarding the imposition of the continuity of displacements and tractions between the elements. One then chooses the $(N+1)$ Lagrange interpolants to the GLL points in order to define a polynomial basis for $\mathbb{P}_N(\Lambda)$. Finally, a simple tensorization rule is applied to generate the higher dimension spaces $\mathbb{P}_N(\Lambda^2)$ and $\mathbb{P}_N(\Lambda^3)$.

To achieve the spatial discretization, the integrals present in Eqs. (35)–(38) are split up into the hexahedra and quadrangles of the spherical mesh. Thanks to the local mappings $\mathscr{F}_\kappa^e$, $\mathscr{F}_l^e$, $\mathscr{G}_{\underline{\kappa}}^e$ and $\mathscr{G}_{\underline{l}}^e$, the elementary integrals can be pulled back to the reference square and cube, where the unknowns and test-functions can be replaced by their polynomial expansions. A numerical quadrature involving the GLL points is then applied to evaluate the integrals on the reference domains Λ^2 and Λ^3.

The procedure outlined above, which is detailed in Appendix B, yields the following system of ordinary differential equations in time:

$$\mathbf{M}_{\mathrm{S}}\mathbf{a} + \mathbf{C}_{\mathrm{S}}\dot{\mathbf{\Phi}} + \mathbf{K}_{\mathrm{S}}\mathbf{d} + \mathbf{B}_{\mathrm{S}}^t\boldsymbol{\lambda}^{\mathrm{S}} = \mathbf{F}, \tag{52}$$

$$\mathbf{B}_{\mathrm{S}}\mathbf{d} = \mathbf{0}, \tag{53}$$

$$\mathbf{M}_{\mathrm{F}}\ddot{\mathbf{\Phi}} + \mathbf{C}_{\mathrm{F}}\mathbf{v} + \mathbf{K}_{\mathrm{F}}\Phi + \mathbf{B}_{\mathrm{F}}^{t}\lambda^{\mathrm{F}} = 0, \tag{54}$$

$$\mathbf{B}_{\mathrm{F}}\dot{\mathbf{\Phi}} = 0, \tag{55}$$

where **d**, **v**, and **a** are the displacement, velocity, and acceleration vectors in the solid, $\boldsymbol{\lambda}^{\mathrm{S}}$ is the traction on the solid–solid boundaries, Φ is the velocity potential in the fluid and λ^{F} is the Lagrange multiplier on the non-conforming fluid–fluid interfaces. **M** is the mass matrix, **K** is the stiffness matrix, **C** is the solid–fluid coupling matrix and **B** is the matrix that computes the jump of any discrete cinematic field across the non-conforming interfaces. Each of the previous matrices has a subscript to indicate on which region (solid or fluid) it operates. In the remaining of the paper, those subscripts will be dropped out whenever there is no possible confusion.

Note that the jump matrices $\mathbf{B}_{\mathrm{S}}$ and $\mathbf{B}_{\mathrm{F}}$ only act on the grid-points which are localized on the non-conforming interfaces. In particular, the equations to be solved at the degrees of freedom interior to the subdomains are obtained by setting $\mathbf{B} = \mathbf{0}$ in Eqs. (52) to (55). An interesting property of the formulation with Lagrange multipliers is that the mass matrices $\mathbf{M}_{\mathrm{S}}$ and $\mathbf{M}_{\mathrm{F}}$ remain diagonal, as for the geometrically conforming case. This is made possible because **M** does not account for the contact condition between subdomains across the non-conforming interfaces.

5. Time evolution

In this section we present an acceleration driven finite-difference scheme that allows for advancing the discrete equations forward in time.

As a starting point, we find more convenient to express the continuity across non-conforming interfaces in terms of the second time derivative of the displacements in the solid and of the potentials in the fluid. We thus replace Eqs. (53) and (55) with:

$$\mathbf{B}_{\mathrm{S}}\mathbf{a} = \mathbf{0}, \tag{56}$$

$$\mathbf{B}_{\mathrm{F}}\ddot{\mathbf{\Phi}} = 0. \tag{57}$$

We then introduce a discretization of the time interval $[0, T]$ into segments of length Δt. For a given integer n, $t_n = n\Delta t$ denotes the n^{th} time step and the subscript n is used to indicate the value of a given vector at time t_n. We start with the initial conditions:

$$\mathbf{F}_{\{n=0\}} = \mathbf{d}_{\{n=0\}} = \mathbf{v}_{\{n=0\}} = \mathbf{a}_{\{n=0\}} = \boldsymbol{\lambda}^{\mathrm{S}}_{\{n=0\}} = \mathbf{0}, \tag{58}$$

$$\Phi_{\{n=0\}} = \dot{\mathbf{\Phi}}_{\{n=0\}} = \ddot{\mathbf{\Phi}}_{\{n=0\}} = \lambda^{\mathrm{F}}_{\{n=0\}} = 0, \tag{59}$$

and we assume that the different fields satisfy Eqs. (52), (54), (56), and (57) at time t_n. Now, for the sake of conciseness the time marching algorithm is presented for the solid regions only. The time evolution for the fluid regions is simply obtained by changing the notations. The issue of coupling the solid and the fluid regions is postponed to the end of this section.

To move forward in time, we use a Newmark finite difference scheme which is based upon the following modified Taylor expansion for the displacement and velocity [64]:

$$\mathbf{d}_{n+1} = \mathbf{d}_n + \Delta t\mathbf{v}_n + \Delta t^2\left[\left(\frac{1}{2} - \beta\right)\mathbf{a}_n + \beta\mathbf{a}_{n+1}\right], \tag{60}$$

$$\mathbf{v}_{n+1} = \mathbf{v}_n + \Delta t[(1-\gamma)\mathbf{a}_n + \gamma\mathbf{a}_{n+1}], \tag{61}$$

with β and γ being two arbitrary scalars. The Newmark scheme is further included into a predictor–multicorrector process as used by Komatitsch and Vilotte [44], but modified to take into account the treatment of the non-conforming interfaces. The different steps of the algorithm are hereafter expanded.

First, the displacements and velocities are predicted by taking the explicit terms in the sequences (60) and (61):

$$\mathbf{d}_{n+1}^{(0)} = \mathbf{d}_n + \Delta t \mathbf{v}_n + \Delta t^2 \left(\frac{1}{2} - \beta \right) \mathbf{a}_n, \tag{62}$$

$$\mathbf{v}_{n+1}^{(0)} = \mathbf{v}_n + \Delta t (1 - \gamma) \mathbf{a}_n, \tag{63}$$

where the superscript between brackets stands for the correction index (0 here). The predicted values of the accelerations and tractions are, respectively, taken to be zero. An acceleration field is then computed by solving the momentum equation. For the grid-points that are not located on the non-conforming interfaces, this reads:

$$\mathbf{a}_{n+1}^{(i+1)} = \mathbf{M}^{-1} \left[\mathbf{F}_{n+1} - \mathbf{K} \mathbf{d}_{n+1}^{(i)} \right], \tag{64}$$

whereas on the interfaces, one has to solve the coupled system:

$$\mathbf{M} \mathbf{a}_{n+1}^{(i+1)} + \mathbf{B}^t \boldsymbol{\lambda}_{n+1}^{(i+1)} = \mathbf{F}_{n+1} - \mathbf{K} \mathbf{d}_{n+1}^{(i)}, \tag{65}$$

$$\mathbf{B} \mathbf{a}_{n+1}^{(i+1)} = \mathbf{0}. \tag{66}$$

Taking the value of the acceleration from (65) and replacing it into (66), we obtain a formulation involving the traction only:

$$\mathbf{B} \mathbf{M}^{-1} \mathbf{B}^t \boldsymbol{\lambda}_{n+1}^{(i+1)} = \mathbf{B} \mathbf{M}^{-1} \left[\mathbf{F}_{n+1} - \mathbf{K} \mathbf{d}_{n+1}^{(i)} \right]. \tag{67}$$

Note that solving the previous equation formally requires the knowledge of the 2D symmetric definite positive matrix $(\mathbf{B} \mathbf{M}^{-1} \mathbf{B}^t)^{-1}$, i.e., a modified mass matrix that accounts for the non-matching grids. This additional resolution step can be performed using a conjugate gradient algorithm with a simple diagonal preconditioner. Then, using the momentum Eq. (65) yields the acceleration field on the non-conforming interfaces:

$$\mathbf{a}_{n+1}^{(i+1)} = \mathbf{M}^{-1} \left[\mathbf{F}_{n+1} - \mathbf{K} \mathbf{d}_{n+1}^{(i)} - \mathbf{B}^t \boldsymbol{\lambda}_{n+1}^{(i+1)} \right]. \tag{68}$$

From Eqs. (64) and (68) the displacements and velocities can finally be corrected:

$$\mathbf{v}_{n+1}^{(i+1)} = \mathbf{v}_{n+1}^{(0)} + \Delta t \gamma \mathbf{a}_{n+1}^{(i+1)}, \tag{69}$$

$$\mathbf{d}_{n+1}^{(i+1)} = \mathbf{d}_{n+1}^{(0)} + \Delta t^2 \beta \mathbf{a}_{n+1}^{(i+1)}. \tag{70}$$

Note that the correction phase only involves the acceleration vector, which by construction, satisfies the continuity constraint (66). The iterative process outlined above thus leads to continuous displacement and velocity fields.

Stability and conservation properties of the scheme as a function of the Newmark parameters β and γ can be found in [64]. A particular example which has been used in this paper is the explicit central finite-difference method (obtained for $\beta = 0$ and $\gamma = 1/2$), which is of second order, conditionally stable and

insures an exact conservation of the total angular momentum. The stability is controlled by the value of the Courant number η, which is defined as $\eta = \Delta t \mathrm{Max}[\alpha/\Delta r]$, where α is the compressional wave speed and Δr is the grid spacing. For the numerical tests presented hereafter, stability was enforced provided that $\eta \leqslant 0.3$.

5.1. Solid–fluid coupling

To couple the solid with the fluid regions requires an additional iterative treatment in order to impose the continuity of both pressure and normal velocity. This coupling is briefly discussed here, but the reader is referred to [49] and the references herein for more details.

For the sake of simplicity let us assume that all the interfaces are conforming. Starting from the predicted values of $\mathbf{d}$, $\mathbf{v}$, Φ, and $\dot{\Phi}$, one gets the acceleration in the solid regions by solving:

$$\mathbf{a}_{n+1}^{(i+1)} = \mathbf{M}_{\mathrm{S}}^{-1}\left[\mathbf{F}_{n+1} - \mathbf{K}_{\mathrm{S}}\mathbf{d}_{n+1}^{(i)} - \mathbf{C}_{\mathrm{S}}\dot{\Phi}_{n+1}^{(i)}\right]. \tag{71}$$

The velocity field in the solid is then updated using (69), and this new value is used to solve for $\ddot{\Phi}$ in the fluid:

$$\ddot{\Phi}_{n+1}^{(i+1)} = \mathbf{M}_{\mathrm{F}}^{-1}\left[-\mathbf{K}_{\mathrm{F}}\Phi_{n+1}^{(i)} - \mathbf{C}_{\mathrm{F}}\mathbf{v}_{n+1}^{(i+1)}\right]. \tag{72}$$

From (72), the first time derivative of the potential can be corrected assuming a relation similar to (69) and it can be injected back into Eq. (71). As noted in [49], this staggered scheme converges after a few number of iterations, typically two for the examples presented in this paper.

5.2. Computational cost

Compared to the geometrically conforming case, the additional resolution step (67) has to be performed to account for the contact conditions between subdomains. Since this is achieved by a conjugate gradient algorithm, the cost of this operation scales as the square of the number of points lying on the the non-conforming interfaces. Let M_{h} stand for the 'horizontal' number of elements used to fill one face of the cubed sphere (for example $M_{\mathrm{h}} = 16$ in Fig. 1), and let M_{v} stand for the number of element layers between the surface of the sphere and the central cube. The cost of the conjugate gradient resolution scales as $N^4 \times M_{\mathrm{h}}^2$, assuming that the polynomial order is $(N-1)$. This is to be compared to the overall cost of the algorithm which is dominated by the product with the stiffness matrix $\mathbf{K}$ and scales as $N^4 \times (M_{\mathrm{h}})^2 \times M_{\mathrm{v}}$ [44]. The relative cost of the non-conforming resolution will, therefore, become marginal as the size of the problem is increased. It will actually scale linearly with the dominant period of the propagating waves.

6. Parallel implementation

The ability of the numerical method presented so far to handle large scale problems is closely related to its properties regarding parallelization. As many finite element method, the SEM yields algorithms that are naturally suited for SIMD implementation on modern parallel calculators, the distribution of tasks being only related to the decomposition of the physical domain. In this section we present a load-balanced partition of the spherical mesh onto a given set of processors and describe the communications required to propagate information within the mesh.

As detailed previously, the spherical mesh is made of a central cube (region 7) which is connected to six external regions (regions 1–6), each region being provided with its own mesh of elements (see Fig. 3). The simplest way for decomposing the global mesh onto a given set of p processors while preserving load

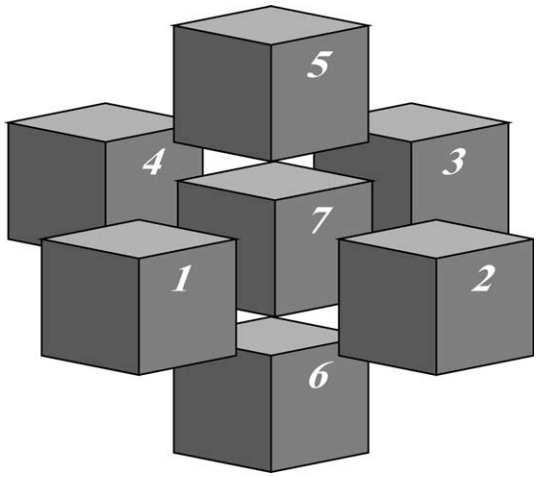

Fig. 3. Schematic view of the topology of the spherical mesh. The central cube (region 7) shares a common face with each of the 6 first regions. The neighboring relations between regions 1 and 6 are not shown on the picture.

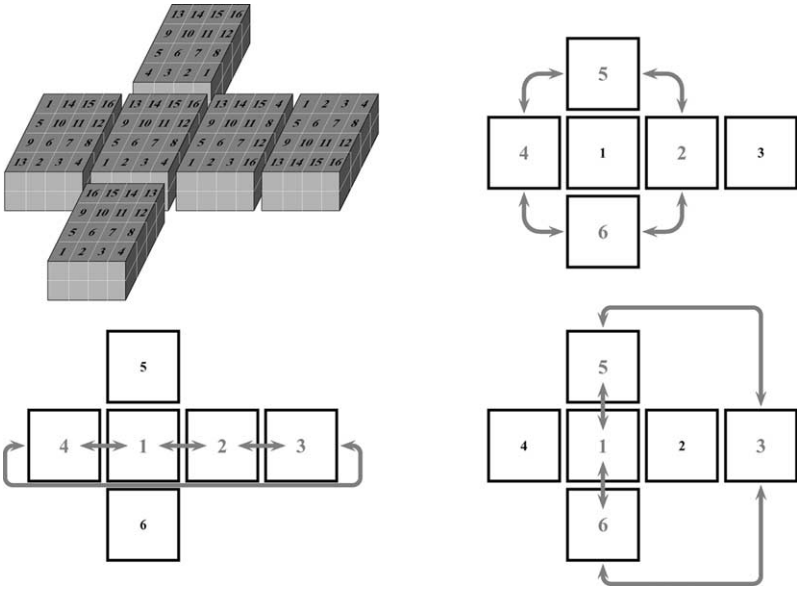

Fig. 4. The top left figure shows the decomposition of the external regions (regions 1–6) onto a set of 16 processors. The remaining figures describe the 3-steps procedure needed to perform the assembly process in the six external regions. Each step is a closed path along the cube's surface which involves the 4 regions whose numbers have been highlighted. The numbering of the subdomains is such that a processor never communicates to itself during the entire operation. In each figure, the regions are represented through a spread view of the 6 faces of a cube with the first region being arbitrarily chosen at the center.

balance is thus to act sequentially on the seven blocks. Note that the strategy used to decompose an external region can be applied to the five others since they are identical to a rotation. On the contrary, the central cube is a particular subset of the mesh which is filled with a number of elements that can differ from the one used in the external regions. Despite this difference, the load attributed to each processor can be easily balanced since each region of the mesh is topologically equivalent to a cube. As an example, Fig. 4 shows a

decomposition of the first six regions onto a set of $p = 16$ processors. Any given external region is cut into 16 vertical slices that extend from the surface of the sphere to the surface of the central cube. The inner cube is further partitioned into 64 regular blocks (not shown on the figure) so that the 2D pattern obtained on the faces of the cube coincide with the slices coming from the external regions. Consequently, each processor is in charge of six subdomains pertaining to the external regions plus 4 subdomains of the inner cube.

Note that the decomposition shown in Fig. 4, is only valid for a number of processors nproc which is the square of a given integer, that is $\text{nproc} = n^2$. In particular, any number of processors which is an even power of two can be used. The generalization to nproc being an odd power of two can be easily performed by separating the first three external regions from the last three. Let indeed p be an even integer, then to split the grid onto $\text{nproc} = 2^{(p+1)}$ processors one would first decompose the regions 1–3 onto a first set of 2^p processors and then decompose the regions 4–6 onto a second set of 2^p processors. Applying the same strategy to the central cube leads to a domain decomposition algorithm well suited to most of the existing parallel computers.

Once the domain decomposition of the sphere has been performed, the processors must communicate to exchange the informations required by neighboring elements. These communications occur when the local expressions of the vector fields involved in the time marching algorithm need to be assembled. The assembly procedure in the spherical mesh is first performed at the region level. Each processor starts with a local assembly within the subdomains it is in charge of, and this step requires no communication. We then make a distinction between the central cube (region 7) and the remaining external regions. In region 7, we use a classical assembly process designed for a structured cube. This step requires three send-get operations to exchange information in the three directions of space (see, e.g. [65]). The assembly phase in the first six regions is based upon the particular topology arising from the use of the cubic-gnomic projection. Recall indeed that the neighboring relations between the external regions goes the same way as between the six faces of a cube. We thus use a sequence of three paths connecting the different regions to ensure a global communication scheme, as shown in Fig. 4. During each of the three steps, all the processors have to communicate to the others. Note, however, that the domain decomposition of the external regions is chosen in such a way that a processor never communicates to itself during the whole process. After the external regions have been assembled, they must be linked to the central cube. This last phase is performed sequentially for each of the six faces of the inner cube. The total communication scheme is thus decomposed into 12 steps: 3 for the central cube, 3 for the external regions and 6 to connect the first six regions to the last one.

The efficiency of the parallel strategy described so far has been measured through a series of experiments. Each of these involves a constant size 3D mesh, the number of processors nproc increasing from 4 to 32. For a given number $\text{nproc} > 4$ of processors, we define the relative efficiency ϵ as:

$$\epsilon = \frac{4}{\text{nproc}} \frac{t(4)}{t(\text{nproc})}, \tag{73}$$

where $t(\text{nproc})$ refers to the time needed to run one time step of the algorithm (62)–(70). The result of these calculations is shown on Fig. 5. The observed efficiency loss is mainly due to the fact that the load attributed to each processor is decreasing, thus affecting the speed-up due to vectorization. Note that the degradation is more gentle for $\text{nproc} = 8$ and $\text{nproc} = 32$ compared to $\text{nproc} = 16$. This is particular to the domain decomposition we use when the number of processors is an odd power of two.

7. Numerical experiments

This section is devoted to the validation of the SEM in spherical geometry through 5 benchmark tests. The first case, which consists of a homogeneous elastic sphere excited by a shallow source, aims at testing the accuracy of the method regarding the propagation of surface waves. Two benchmarks are then pro-

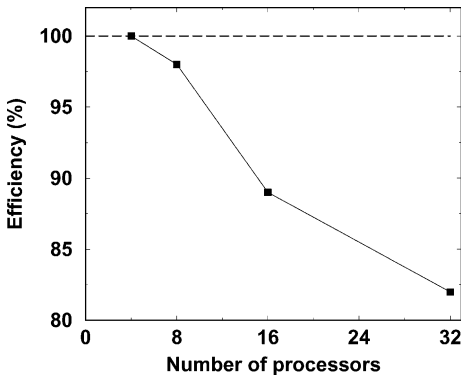

Fig. 5. Parallel efficiency measured for nproc = 4, 8, 16, and 32.

posed in order to check the implementation of a geometrically non-conforming interface: the homogeneous elastic case and a two-layers sphere in which each layer has its own discretization. The effects of gravity are eventually included, first in a homogeneous solid sphere and then in a model with a neutrally stratified fluid outer core.

In each case, the normal mode solution [66–68] is taken as a reference. We systematically use a double-couple source which time dependence is the second derivative of a Gaussian bell. The reader is referred to [44] for a presentation of how to incorporate a double-couple source in the SEM. Except for the last example, the central frequency of the source is $f_0 \simeq 2.7$ mHz, its maximal frequency (i.e., the frequency for which the power spectrum equals 5% of its maximum) is $f_c \simeq 6.75$ mHz and the time onset is $T_0 \simeq 550$ s. The radius of the sphere is chosen to be that of the Earth, i.e., 6371 km and the total simulation time, when not mentioned explicitly, is 8640 s (i.e., 144 min).

7.1. Conforming grid

As a first experiment we consider a homogeneous elastic sphere that is excited by an explosive source located close to the surface, at depth $\simeq$63 km. The spectral element mesh is kept conforming in order to test the spherical transformation and the communication strategy described in the previous section.

The P-wave velocity is $\alpha = 8000$ m s^{-1}, the S-wave velocity is $\beta = 6000$ m s^{-1} and the density is $\rho = 3000$ kg m^{-3}. The dominant P wavelength is about half the radius of the sphere and the shortest S wavelength is about 2200 km. We use a polynomial degree $N = 8$ and a minimal number of 5 grid-points per wavelength following previous studies [44,69]. In this particular example, it is the Rayleigh wave that is expected to travel with the smallest (group) velocity thus, when imposing the "5 points criterion" we refer to a minimal velocity of 5000 m s^{-1}. The global mesh is built following the method explained previously with the size of the central cube being 2742 km. Each external region (regions 1–6) is discretized with 4 elements in the radial direction and 8×8 elements in the tangential direction, while the central cube is filled with $8 \times 8 \times 8$ elements. The resulting 3D mesh contains a total number of 2048 elements and the smallest length between two grid-points is about 34 km. The time step is $\Delta t = 0.5$ s which corresponds to a Courant number $\eta \simeq 0.23$.

Fig. 6 shows the displacement recorded at the grid-points that stand at the surface of the sphere along the Equator. The vertical "stripes" seen on the plot are due to the uneven distribution of GLL points on the reference unit cube. Only the radial (vertical) and longitudinal components of the displacement field are shown since (a) the explosive source does not generate toroidal energy and (b) the spheroidal energy does not appear on the transverse component when an explosive source is considered.

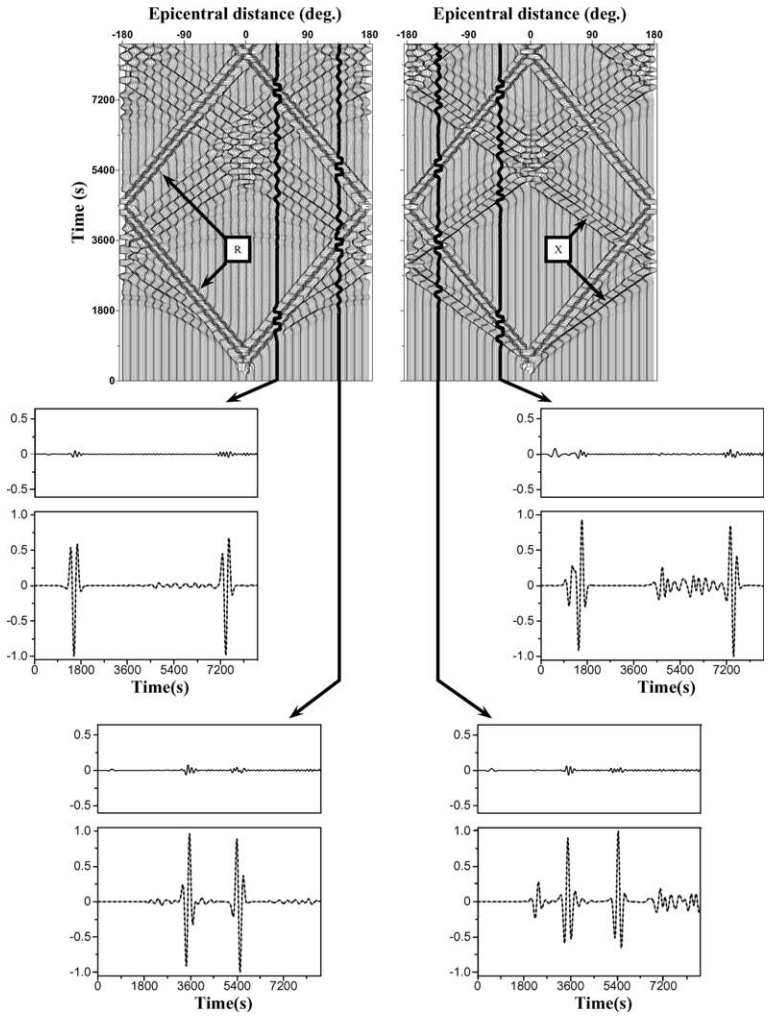

Fig. 6. Radial (left panel) and longitudinal (right panel) displacements recorded at the surface of a homogeneous elastic sphere. The whole seismograms are displayed above, for amplitudes less than 85% of their maximal value. The almost non-dispersive Rayleigh wave (R) is labeled on the radial component and the X wave (X) is identified on the longitudinal component. Individual normalized traces (dashed line) and their comparison to a normal mode solution (solid line) are shown at epicentral distances $\Delta = 45°$ (middle) and $\Delta = 135°$ (bottom). For each of the four plots, the top curve shows the difference between the two solutions amplified by a factor of 10.

The Rayleigh wave (R) is observed on both components and exhibits an elliptic polarization in the great circle plane. Its apparent group velocity is almost constant and close to 5000 m s^{-1}. Surprisingly, observation at a grazing angle of the Rayleigh pulse reveals no clear difference between group and phase velocity. The Rayleigh wave is thus almost non-dispersive despite the fact that the free-surface is curved. Physical dispersion of the Rayleigh wave is nonetheless expected to occur at frequencies lower than those considered here [70].

The second ''surface wave'' labeled on the plot is the X wave [71], which can be viewed as the limit of multiple reflections and conversions of P and SV waves under the surface of the sphere. For example, the impulsive energy arrival which is clearly seen on the longitudinal component before 2700 s results from multiple underside P reflections off the surface. Its polarization is thus tangent to the surface and its ap-

parent group velocity is close to the P-wave velocity in the medium. After a complete orbit around the surface of the sphere, note that the shape of the X pulse has broadened due to the progressive excitation of the different phases forming the X wave.

The largest amplitudes in the seismograms are due to refocusing of surface waves in the vicinity of the antipode and the epicenter. Furthermore, each time the Rayleigh or the X wave pulses reach the antipode or return back to the epicenter, they experience a $\pi/2$ phase shift that reverts their signal in time. This is expected since both the epicenter and the antipode act as caustics for waves traveling on the surface of a sphere [72,73].

The comparison of single traces to the normal mode solution is shown in the bottom panel of Fig. 6. The residual between the SEM calculations and the reference solution is less than 1%. The largest values are reached for the Rayleigh wave pulse which is related to the slowest velocity in the medium. In that case the residuals are explained by a small time shift induced by the finite difference scheme which is (only) of order two.

7.2. Non-conforming grids

7.2.1. Homogeneous sphere

This experiment is similar to the previous one except that the source depth is set to 1187 km and we coarsen the mesh by a factor of two at a depth of 2500 km. The source is deeper than in the conforming case since most of the energy excited by a shallower source would travel as surface waves that could hardly "feel" the lower part of the grid. The 3D mesh contains a total number of 1048 elements and the time step is $\Delta t = 1$ s, which is twice as big as for the conforming case while the Courant number is unchanged. The conjugate gradient resolution of Eqs. (65) and (66) required an average of 8 iterations for each time step to decrease the acceleration jump of about 5 orders of magnitude. For the particular mesh used in this experiment, the amount of time devoted to the treatment of the non-conforming interface represents about 40% of the total calculation time. This proportion is expected to diminish for simulations at higher frequency since, as mentioned previously, the ratio between the number of points on the non-conforming interface and the total number of grid-points decreases as the frequency increases.

The displacement field recorded at the surface of the sphere is shown in the top panel of Fig. 7. Both the Rayleigh wave and the X wave can be identified in the plot because of the low frequency content of the source. However, a significant amount of energy is transported in the medium by body waves. The first energy arrival which is seen at every receiver at the surface is the direct P wave which is radially polarized at the antipode (i.e., for $\Delta = \pm 180°$). The PP wave (P wave reflected at the surface) is recorded just beneath the source at $t \simeq 3600$ s. Higher order underside reflections off the surface (PPP, $PPPP$, etc.) are difficult to identify due to interferences with the other body and surface waves. The bottom panel of Fig. 7 shows the comparison of individual traces with the reference normal mode solution. The agreement between the two solutions is very satisfying since their relative difference only reaches a few percents.

Fig. 8 shows the variation of kinetic and potential energy calculated at the discrete level during the simulation. The main conversions between kinetic and potential energy occur when elastic waves are reflected at the surface or when surface waves interfere at the antipode. The conservation of the total energy indicates that no spurious reflections are generated at the non-conforming interface.

The correct treatment of the non-conforming interfaces is controlled by the number of iterations in the conjugate gradient algorithm, N_{iter}, and by the time step used in the simulation, Δt. Both parameters control the satisfaction of the continuity constraint (56). Whenever this constraint is violated, the non-conforming interfaces act as secondary sources that bring energy to the whole system. The relative influence of N_{iter} and Δt on the total energy variation is shown on Fig. 9. We find that increasing the number of iterations by two units is more efficient that dividing the time step by a factor of two. On the one hand, this confirms that N_{iter} is a key parameter that governs the accuracy of the treatment of the non-conforming interfaces. On the

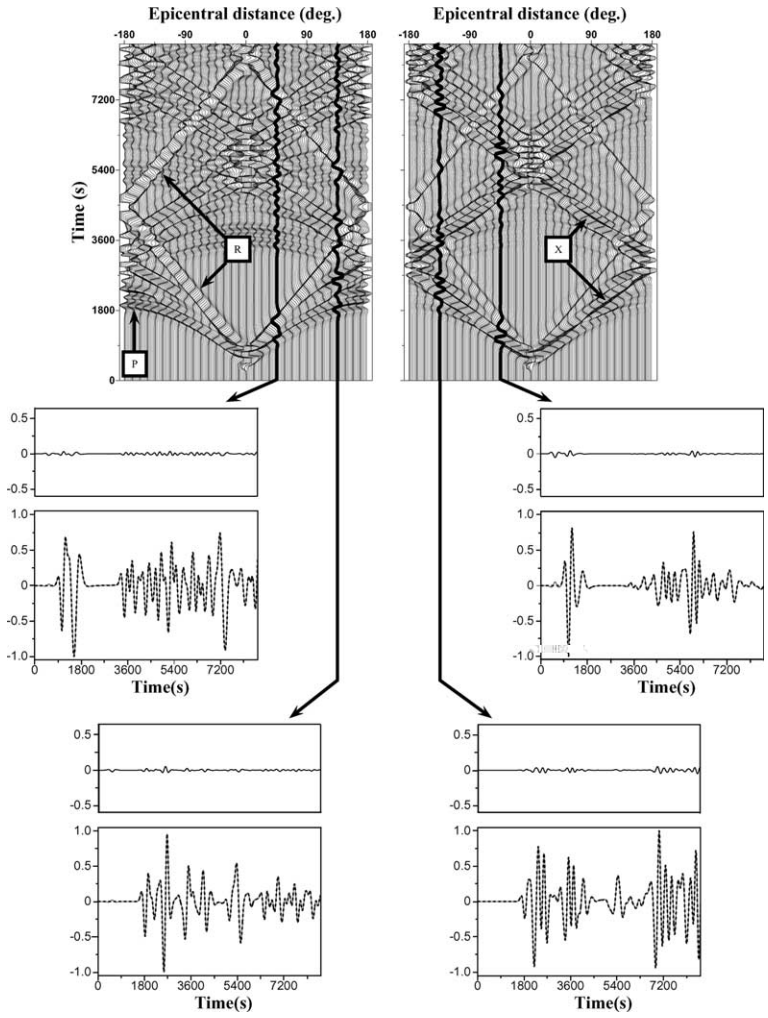

Fig. 7. Radial (left panel) and longitudinal (right panel) displacements recorded at the surface of a homogeneous elastic sphere discretized with non-conforming grids. The whole seismograms are displayed above, for amplitudes less than 85% of their maximal value. Both the Rayleigh wave R and the P wave (P) are labeled on the radial component and the X wave (X) is identified on the longitudinal component. Individual normalized traces (dashed line) and their comparison to a normal mode solution (solid line) are shown at epicentral distances $\Delta = 45°$ (middle) and $\Delta = 135°$ (bottom). The top curves show the difference between the two solutions amplified by a factor of 10.

other hand, this also suggests that this treatment does not degrade the order of the time marching algorithm.

7.2.2. 2-Layers elastic sphere

The aim of this experiment is to validate the implementation of a non-conforming interface that coincides with a physical interface. The 3D mesh of spectral elements is the same as for the non-conforming homogeneous case. An explosive source depth is set at 1312 km depth and a 10% decrease in both S and P velocity is implemented at 2500 km depth across the non-conforming interface. The medium is thus formed by a homogeneous sphere of radius 3871 km surrounded by a homogeneous spherical shell with different

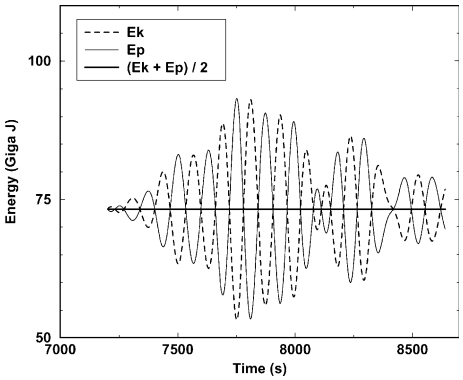

Fig. 8. Evolution of kinetic (E_k) and potential (E_p) energy during the last 20 min of the simulation. The total energy is conserved indicating a correct treatment of the non-conforming interfaces in the numerical discretization.

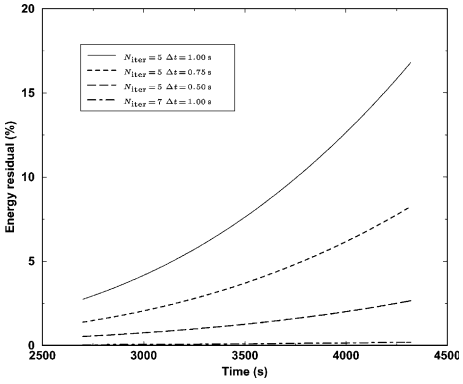

Fig. 9. Influence of the number of iterations N_{iter} in the conjugate gradient algorithm and of the time step Δt on the variation of the total energy.

elastic properties. The density is increased by a factor of 3 in the inner part of the model so that the impedance contrast for both P and S waves is much larger than one. We thus expect to test the non-conforming implementation when strong reflections are generated at the inner boundary. Because the velocities decrease with depth, the same time step as for the homogeneous non-conforming case ($\Delta t = 1$ s) can be used and results in an even smaller Courant number, $\eta \simeq 0.21$. We found that an average number of 5 iterations in the conjugate gradient algorithm was sufficient to decrease the acceleration jump across the non-conforming interface by 5 orders of magnitude (compared to 8 iterations in the homogeneous case).

A complete study of how the number of iterations depends on the elastic properties of the medium has not been carried out here, but the following rule of thumb can be given. If no iterations are done, then the non-conforming interface would act as a free, totally reflecting surface. Conversely, in a homogeneous medium the interface must transmit all the energy from one subdomain to the other. In this case a maximum number of iterations, say N_H, is expected during the resolution of Eqs. (65) and (66) in order to get the correct physical behavior. A physical non-conforming interface will thus appear as an intermediate case between these extrema and will require a number of iterations ranging between zero and N_H.

Fig. 10 displays the seismograms in displacement recorded at the surface of the 2-layers sphere. As expected the displacement field is dominated by reverberations in the outer spherical shell which give the

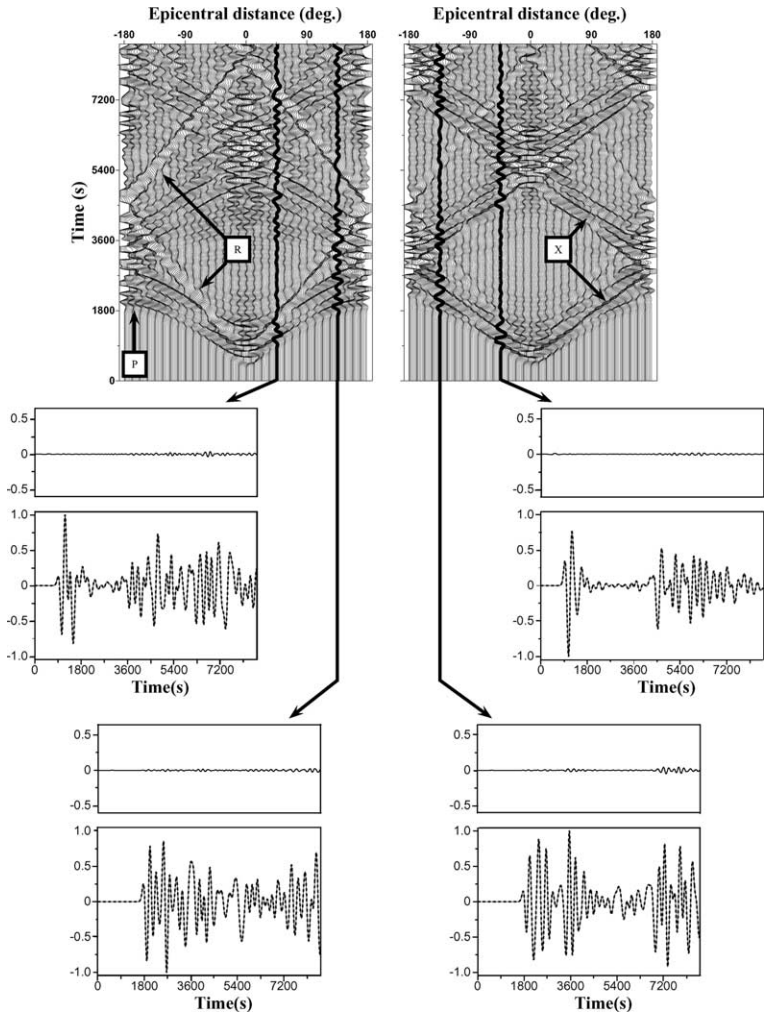

Fig. 10. Radial (left panel) and longitudinal (right panel) displacements recorded at the surface of a 2-layers elastic sphere discretized with non-conforming grids. The whole seismograms are displayed above, for amplitudes less than 85% of their maximal value. Both the Rayleigh wave (R) and the P wave (P) are labeled on the radial component and the X wave (X) is identified on the longitudinal component. Individual normalized traces (dashed line) and their comparison to a normal mode solution (solid line) are shown at epicentral distances $\Delta = 45°$ (middle) and $\Delta = 135°$ (bottom). The top curves show the difference between the two solutions amplified by a factor of 10.

main seismic phases (P, PP, R) a "ringing" aspect. This is also clearly seen on individual traces for epicentral distances $\Delta = 45°$ and $\Delta = 135°$ (compare with bottom panel of Fig. 7). The agreement between the SEM results and the normal mode calculations is again satisfying since the magnitude of the residuals remain within a few percents of the reference solution.

7.3. Gravity effects

The results presented so far did not take into account the gravity terms in the expression of the bilinear form (41). Gravity is known to play a non-negligible role on the propagation of surface waves

in the Earth at periods longer than about 30 s [3]. To illustrate this behavior, we consider a homogeneous self-gravitating solid sphere which is excited by a shallow ($\simeq$63 km) strike-slip source. The 3D mesh is identical to the one used for the non-conforming homogeneous elastic case and the time step is again $\Delta t = 1$ s.

Fig. 11 shows the displacements recorded at the surface and their comparison to the purely elastic solution at epicentral distances ranging from $\Delta = 110°$ to $\Delta = 170°$. Since each couple of traces is normalized individually, the focusing of both the Rayleigh wave and the X wave near the antipode is not apparent in the plot.

The main feature observed in the top panel of Fig. 11 is the decrease of the Rayleigh wave group velocity together with a slight phase shift of the Rayleigh pulse. For example, the second arrival (R_2) is delayed by about 50 s at an epicentral distance $\Delta = 110°$, which corresponds to a diminution of 0.85% with respect to a reference group velocity of 5000 m s^{-1}. Surprisingly, an opposite effect is observed on the X wave, that is a

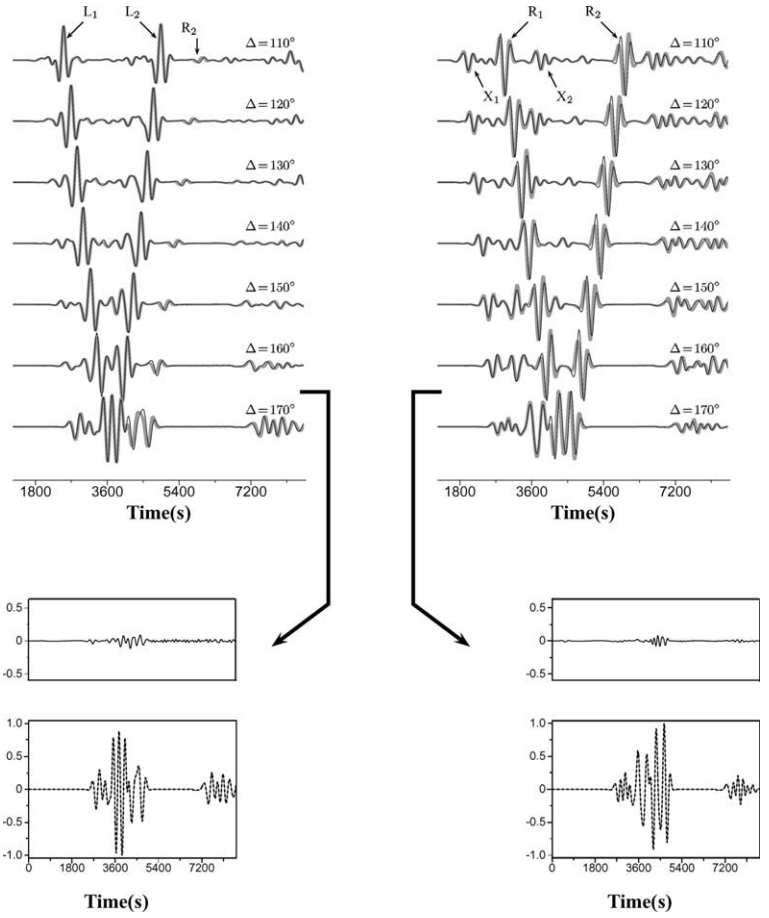

Fig. 11. The top panel shows the transverse (left) and longitudinal (right) surface displacements recorded in a homogeneous sphere in the elastic case (bold gray lines) and considering gravity (thin black lines). Gravity causes the Rayleigh wave group velocity to decrease, the X wave to be slightly accelerated while it does not affect the Love wave. The first two orbits of these surface waves are labeled R_1, R_2, X_1, X_2, L_1, and L_2, respectively. The bottom panel compares the results obtained by the SEM (dashed line) to the normal mode solution (solid line) at epicentral distance $\Delta = 168.75°$ for both transverse (left) and longitudinal (right) components. The difference between the two solutions amplified by a factor of 10 is displayed above the individuals traces.

slight apparent velocity increase in presence of gravity. At a distance of $\Delta = 110°$ the first energy arrival in the X_2 pulse has indeed a 15 s advance with respect to the elastic reference pulse. This results in an increase of about 0.40% with respect to a reference group velocity of 8000 m s^{-1}. However, it seems that gravity affects the seismic phases forming the X wave in a different way and a global time shift is hardly observed on the entire X pulse. Eventually, the Love waves are unaffected by gravity as it is expected from their pure toroidal nature.

The bottom panel of the figure shows the comparison of the SEM results to the reference normal mode solution at an epicentral distance of $\Delta \simeq 169°$. The residuals have the same magnitude as for the homogeneous elastic case (compare with Fig. 6) and do not exceed a few percents of the reference solution.

7.4. Fluid outer core

As a last example, we consider a model having a homogeneous solid inner core with radius 1371 km, a heterogeneous fluid outer core and a 2500 km thick homogeneous solid mantle. The variation with depth of the elastic parameters as well as the density are shown in Fig. 12. The density increases from 7000 kg m^{-3} in the mantle to 9000 kg m^{-3} in the inner core. From this density profile we build a P-velocity model for which the Brunt–Väisälä frequency is exactly zero. This is done by first computing $\mathbf{g}$ from Poisson's equation and then solving (13) for c. The P-velocity values at the boundaries of the outer core are then extrapolated to the mantle and to the inner core. The S-velocity model is obtained after assuming that the solid parts of the model are Poisson solids, i.e., with $\lambda = \mu$ or $\alpha = \sqrt{3}\beta$.

Note that the variation of the P-velocity is highly unrealistic in the model of Fig. 12. However, a neutrally stratified outer core is certainly a reasonable assumption for the Earth, given the actual resolution of density in global tomographic models [74].

The spectral element grid we use has a non-conforming interface in the fluid outer core at 3750 km depth. The source time function is the second derivative of a Gaussian with a dominant frequency $f_0 = 1$ mHz, and the time step is $\Delta t = 1$ s. Such a low frequency source is expected to generate very long period surface waves with a non-negligible sensitivity to the structure of the outer core. Since gravity only affects surface waves, this provides a reliable test for validating the implementation of gravity in the fluid.

Fig. 13 shows the surface displacement field obtained for an explosive source set at 147-km depth. The seismograms exhibit a strongly dispersive Rayleigh wave, with an apparent group velocity close to 5000 m s^{-1}. As discussed previously, the dispersive nature of the Rayleigh pulse arises because its dominant

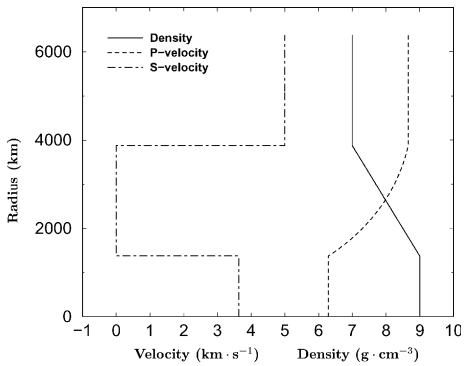

Fig. 12. Variation with depth of the density (solid line), the P-velocity (dashed line) and the S-velocity (dot-dashed line) for the fluid–solid model considered in this paper. Both the inner core and the mantle are homogeneous Poisson solids whereas the fluid outer core is heterogeneous, neutrally stratified.

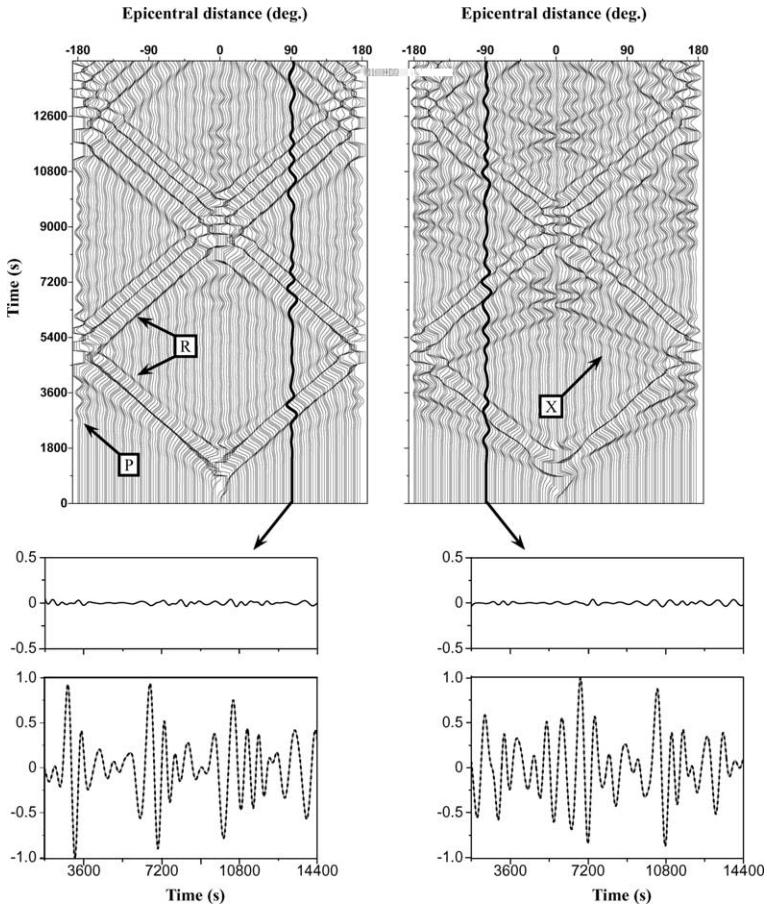

Fig. 13. The top panel shows the radial (left) and longitudinal (right) surface displacements recorded in the model of Fig. 12 for a shallow explosive source. Amplitudes larger than 95% of the maximal value have been clipped. The different labels refer to the Rayleigh (R) and X (X) surface waves and to the first (P) arrival. The bottom panel compares the results obtained by the SEM (dashed line) to the normal mode solution (solid line) at epicentral distance $\Delta = 90°$ for both radial (left) and longitudinal (right) components. The difference between the two solutions amplified by a factor of 10 is displayed above the individuals traces.

wavelength is now comparable to the curvature of the free surface. Only the first P arrival as well as the surface X wave can be clearly identified at those frequencies, and have been labeled on the plot.

The comparison of individual traces with the reference normal mode solution is shown in the bottom of Fig. 13. The match is found to be satisfying on both the radial and the longitudinal components, since the residuals are close to 1% throughout the simulation, which is 4 h long.

Another feature of interest, related to the presence of the fluid outer core, is the excitation of a Stoneley wave at the core-mantle boundary (CMB). Although Stoneley waves are never recorded at the surface of the Earth, they provide a demanding validation test to the fluid–solid coupling strategy presented in this paper.

Fig. 14 shows the displacement field recorded at the CMB for an explosive source located close to the fluid–solid boundary, at 2437-km depth. A strongly dispersive Stoneley wave is clearly seen on the radial component, with an apparent group velocity close to the Rayleigh wave group velocity. The comparison of the SEM results to the reference solution shows a very good agreement, as the residuals reach only a few percents at the end of the simulation.

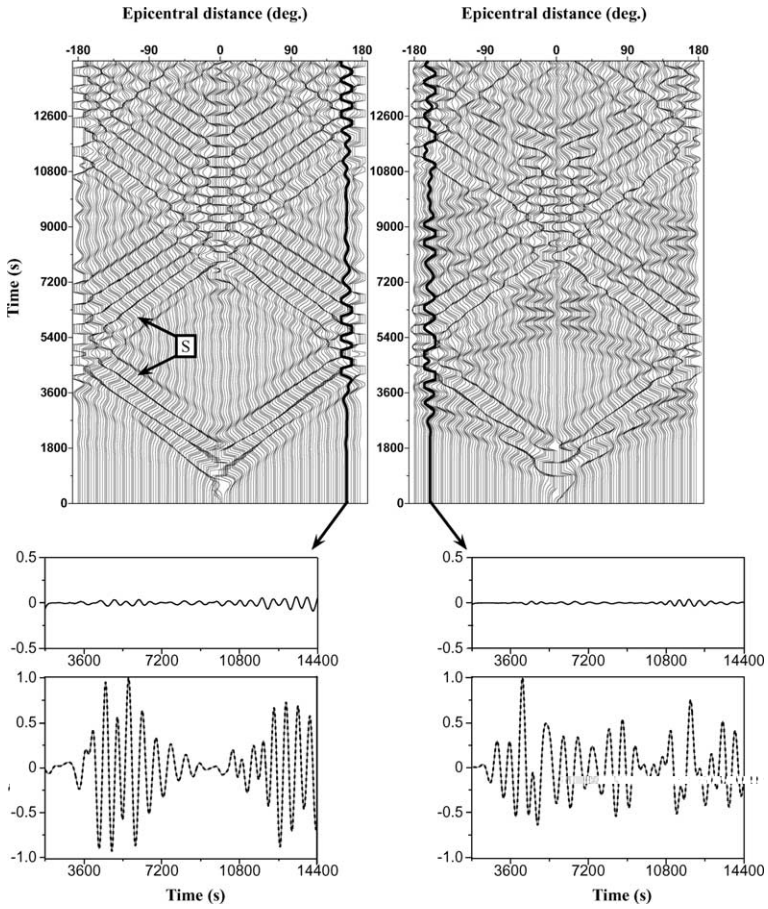

Fig. 14. The top panel shows the radial (left) and longitudinal (right) displacements recorded at the core-mantle boundary in the model of Fig. 12 for a deep explosive source. Amplitudes larger than 90% of the maximal value have been clipped. The dispersive Stoneley wave (S) is labeled on the radial component. The bottom panel compares the results obtained by the SEM (dashed line) to the normal mode solution (solid line) at epicentral distance $\Delta \simeq 160°$ for both radial (left) and longitudinal (right) components. The difference between the two solutions amplified by a factor of 10 is displayed above the individuals traces.

8. Conclusions

We have presented a parallel spectral element approximation to the elastic wave equation in an isotropic solid–fluid sphere, accounting for the effects of gravity within the Cowling approximation and assuming a neutrally stratified fluid. The method is based upon a non-conforming paving of the sphere which enables to adapt the grid-points sampling with depth. We have presented the results of a few benchmark tests for radial models of elastic parameters, that illustrate the accuracy of the method. In particular, it has been shown that the propagation of surface and interface waves is successfully modeled, even in the case of a strong physical dispersion. Future work will focus on including the rotation as well as a complete implementation of self-gravitation, i.e., with mass re-distribution. The method can readily be adapted to laterally heterogeneous models, for which numerical experiments should help to provide a better understanding of 3D wave propagation in planetary interiors.

Acknowledgements

We thank Bernard Valette for numerous discussions about the variational formulation of the self-gravitation equations, and Christine Bernardi and Yvon Maday for introducing us to the mortar element method. We acknowledge Dimitri Komatitsch for fruitful discussions about the solid–fluid coupling, and Jeroen Tromp for kindly providing his mode summation code. The writing of this manuscript has benefited from the careful reading of Alexandre Fournier. The calculations presented in this paper were performed both at the Institut de Physique du Globe de Paris (on a cluster of 8 ES40, each with four 500 MHz Compac-EV6 processors) and at the Geosciences department of Princeton University, on H.-P. Bunge's geowulf (a cluster of 64 biprocessors Intel Pentium-II with 350 MHz CPU). The cluster at IPGP was funded by the french MENRT, CNRS, and région Ile-de-France.

Appendix A. Transition between a 2-sphere and a cube

Consider a 2-sphere with radius a and a cube which half-length is b, both of them being centered on the origin of a Cartesian coordinates system. It is assumed that the cube lies inside the sphere, that is $\sqrt{3}b < a$. As a starting point, the volume comprised between the sphere and the inner cube is decomposed into six regions, each of these being a deformed cube with its upper face leaning on the 2-sphere (see Fig. 2). Let (ξ, η, γ) be the generic vector on the reference unit cube $\Lambda^3 = [-1, 1]^3$. We hereafter define for each region of the mesh, the transformation from (ξ, η, γ) to the Cartesian coordinates (x, y, z). Following Ronchi et al. [31], we first introduce the auxiliary variables:

$$X = \tan\left(\frac{\pi}{4}\xi\right), \tag{A.1}$$

$$Y = \tan\left(\frac{\pi}{4}\eta\right), \tag{A.2}$$

$$\delta = \left(1 + X^2 + Y^2\right)^{-(1/2)}, \tag{A.3}$$

$$\Psi = \frac{\gamma + 1}{2}. \tag{A.4}$$

Inside a given region Ψ spans the interval $[0, 1]$, with $\{\Psi = 0\}$ corresponding to the surface of the inner cube and $\{\Psi = 1\}$ to the 2-sphere. The value of Ψ is used to define a linear transition from the cubed sphere mapping [31] to the Cartesian metric inside the inner cube. The analytical expression for this transformation writes:

Region 1 ($x > 0$)	Region 2 ($y > 0$)	Region 3 ($x < 0$)
$x = a\delta\Psi + b(1 - \Psi)$ $y = x[X\Psi + \xi(1 - \Psi)]$ $z = x[Y\Psi + \eta(1 - \Psi)]$	$x = -y[X\Psi + \xi(1 - \Psi)]$ $y = a\delta\Psi + b(1 - \Psi)$ $z = y[Y\Psi + \eta(1 - \Psi)]$	$x = -a\delta\Psi - b(1 - \Psi)$ $y = x[X\Psi + \xi(1 - \Psi)]$ $z = -x[Y\Psi + \eta(1 - \Psi)]$
Region 4 ($y < 0$)	**Region 5 ($z > 0$)**	**Region 6 ($z < 0$)**
$x = -y[X\Psi + \xi(1 - \Psi)]$ $y = -a\delta\Psi - b(1 - \Psi)$ $z = -y[Y\Psi + \eta(1 - \Psi)]$	$x = -z[Y\Psi + \eta(1 - \Psi)]$ $y = z[X\Psi + \xi(1 - \Psi)]$ $z = a\delta\Psi + b(1 - \Psi)$	$x = -z[Y\Psi + \eta(1 - \Psi)]$ $y = -z[X\Psi + \xi(1 - \Psi)]$ $z = -a\delta\Psi - b(1 - \Psi)$

As for the cubed sphere mapping, the metric tensor arising from this transformation is identical in each region. But its non-diagonal terms are a priori non-zero, implying that the lines within the mesh are not orthogonal. Finally, note that setting Ψ to 1 in the previous formulae provides the analytic expression to obtain a cubed sphere of radius a.

Appendix B. SEM discretization

In this annex we detail the main features of the SEM approximation of the wave equation, restricting ourselves to the solid regions. The reader is referred to [40] and [75] for a complete presentation of the spectral element method.

B.1. Numerical integration

The numerical integration rule is based upon the Gauss–Lobatto–Legendre (GLL) points, which are defined on the reference 1D element $\Lambda = [-1, 1]$ by:

$$\xi_0^N = -1; \quad \xi_N^N = 1; \quad L'_N(\xi_i^N) = 0 \quad \forall i \in \{1, \ldots, N-1\}, \tag{B.1}$$

where L'_N stands for the derivative of the Legendre polynomial of degree N. On the reference unit segment Λ, the numerical integration formula provided by the $(N+1)$ GLL points is exact until polynomial order $(2N-1)$:

$$\int_\Lambda q(\xi)\mathrm{d}\xi = \sum_{i=0}^{N} \rho_i^N q(\xi_i^N) \quad \forall q \in \mathbb{P}_{2N-1}(\Lambda). \tag{B.2}$$

In the previous formula, the $(N+1)$ scalars ρ_i^N are the integration weigths defined as:

$$\rho_i^N = \int_\Lambda h_i^N(\xi)\mathrm{d}\xi, \tag{B.3}$$

with $(h_i^N, i = 0 \ldots N)$ standing for the Lagrange polynomials of order N related to the $(N+1)$ GLL points:

$$h_i^N(\xi_j^N) = \delta_{ij} \quad \forall (i,j) \in \{0, \ldots, N\}^2, \tag{B.4}$$

where δ is the Kronecker delta. Making use of Eq. (B.2) in each space direction, it is straightforward to define a numerical integration rule on the unit square Λ^2 or cube Λ^3. The integral of a given scalar field q defined on the unit cube will thus be approximated by:

$$\int_{\Lambda^3} q(\boldsymbol{\xi})\mathrm{d}\boldsymbol{\xi} \simeq \sum_{i=0}^{N}\sum_{j=0}^{N}\sum_{k=0}^{N} q(\xi_i^N, \xi_j^N, \xi_k^N)\rho_i^N\rho_j^N\rho_k^N, \tag{B.5}$$

where $\boldsymbol{\xi}$ stands for the generic vector on Λ^3. Note that the integration rule defined by (B.5) is only exact for tensorized polynomials pertaining to $\mathbb{P}_{2N-1}(\Lambda) \otimes \mathbb{P}_{2N-1}(\Lambda) \otimes \mathbb{P}_{2N-1}(\Lambda)$.

We will hereafter write $\oint_{\Lambda^\alpha}^N$ to refer to the numerical integration based upon the $\alpha(N+1)$ GLL points on the reference element Λ^α. For example, the right hand side of Eq. (B.5) will be denoted $\oint_{\Lambda^3}^N q(\boldsymbol{\xi})$.

B.2. Polynomial basis

In order to construct the discrete spaces $\mathscr{V}_{\mathrm{h}}^{\mathrm{S}}$ and $\mathscr{M}_{\mathrm{h}}^{\mathrm{S}}$ defined by Eqs. (48) and (50), one needs to provide basis for the polynomial spaces $\mathbb{P}_N(\Lambda^2)$ and $\mathbb{P}_N(\Lambda^3)$. In the SEM, these basis are formed by tensor product of the Lagrange interpolants related to the GLL points on Λ as defined by Eq. (B.4). Let for example $\mathbf{w}$

stand for an admissible displacement field with Cartesian components $\left(w_\beta\right)_{\beta=1,3}$. To compute the value of w_β at the grid point $(x,y,z)=\mathscr{F}^e_\kappa(\xi,\eta,\gamma)$ on τ^e_κ, one writes:

$$w_\beta(x,y,z)=w_\beta|\tau^e_\kappa\circ\mathscr{F}^e_\kappa(\xi,\eta,\gamma)=\sum_{i=0}^{N}\sum_{j=0}^{N}\sum_{k=0}^{N}w_\beta(x_i^{\kappa,e},y_j^{\kappa,e},z_k^{\kappa,e})h_i^N(\xi)h_j^N(\eta)h_k^N(\gamma), \tag{B.6}$$

where $(x_i^{\kappa,e},y_j^{\kappa,e},z_k^{\kappa,e})$ are the collocation points on τ^e_κ:

$$(x_i^{\kappa,e},y_j^{\kappa,e},z_k^{\kappa,e})\doteq\mathscr{F}^e_\kappa(\xi_i^N,\xi_j^N,\xi_k^N). \tag{B.7}$$

B.3. Scalar product and bilinear forms

The $\mathbf{L}^2(\Omega^{\mathrm{S}})$ scalar product between two admissible displacement fields $\mathbf{v}$ and $\mathbf{w}$ writes:

$$\int_{\Omega^{\mathrm{S}}}\mathbf{v}(\mathbf{x})\cdot\mathbf{w}(\mathbf{x})\mathbf{dx}=\sum_{\kappa=1}^{K}\sum_{e=1}^{n_\kappa}\int_{\tau^e_\kappa}\mathbf{v}(\mathbf{x})\cdot\mathbf{w}(\mathbf{x})\mathbf{dx}. \tag{B.8}$$

Each elementary integral can then be expressed on the reference cube via the local transformation $\mathscr{F}^e_\kappa$:

$$\int_{\tau^e_\kappa}\mathbf{v}(\mathbf{x})\cdot\mathbf{w}(\mathbf{x})\mathbf{dx}=\int_{\Lambda^3}\mathbf{v}^{\kappa,e}(\boldsymbol{\xi})\cdot\mathbf{w}^{\kappa,e}(\boldsymbol{\xi})|\mathscr{J}^e_\kappa|(\boldsymbol{\xi})\mathbf{d}\boldsymbol{\xi}, \tag{B.9}$$

where $\mathbf{v}^{\kappa,e}\doteq\mathbf{v}_{|\tau^e_\kappa}\circ\mathscr{F}^e_\kappa$, $\mathbf{w}^{\kappa,e}\doteq\mathbf{w}_{|\tau^e_\kappa}\circ\mathscr{F}^e_\kappa$ and $\mathscr{J}^e_\kappa$ is the Jacobian matrix related to $\mathscr{F}^e_\kappa$. Applying the numerical integration rule (B.5) to the previous equation yields the final expression for the approximated scalar product:

$$(\mathbf{v},\mathbf{w})_{\mathrm{h}}=\sum_{\kappa=1}^{K}\sum_{e=1}^{n_\kappa}\oint_{\Lambda^3}^{N}|\mathscr{J}^e_\kappa|[\mathbf{v}^{\kappa,e}\cdot\mathbf{w}^{\kappa,e}](\boldsymbol{\xi})\quad\forall(\mathbf{v},\mathbf{w})\in\mathscr{V}^{\mathrm{S}}_{\mathrm{h}}\times\mathscr{V}^{\mathrm{S}}_{\mathrm{h}}. \tag{B.10}$$

Note that the numerical integration involved in (B.10) is never exact since the integrated quantity $\mathbf{v}^{\kappa,e}\cdot\mathbf{w}^{\kappa,e}$ is already in $\mathbb{P}_{2N}(\Lambda^3)$.

The approximation of the bilinear form $\mathscr{A}^{\mathrm{S}}$ goes the same way, except for the differential operators that are involved in Eq. (41). To take this difference into account, we introduce the modified operators on the unit cube:

$$\tilde{\nabla}\phi^{\kappa,e}(\boldsymbol{\xi})\doteq\nabla\phi(\mathbf{x}), \tag{B.11}$$

$$\tilde{\nabla}\mathbf{v}^{\kappa,e}(\boldsymbol{\xi})\doteq\nabla\mathbf{v}(\mathbf{x}), \tag{B.12}$$

$$\tilde{\nabla}\cdot\mathbf{v}^{\kappa,e}(\boldsymbol{\xi})\doteq\nabla\cdot\mathbf{v}(\mathbf{x}), \tag{B.13}$$

where $\mathbf{x}=\mathscr{F}^e_\kappa(\boldsymbol{\xi})$ and where $\tilde{\nabla}$ denotes spatial derivation with respect to the $\boldsymbol{\xi}$ coordinate. Expressing the integrals of Eq. (41) back onto the unit cube and using the numerical integration (B.5) yields the final expression for $\mathscr{A}^{\mathrm{S}}_{\mathrm{h}}$:

$$\begin{aligned}\mathscr{A}^{\mathrm{S}}_{\mathrm{h}}(\mathbf{v},\mathbf{w})=&\sum_{\kappa=1}^{K}\sum_{e=1}^{n_\kappa}\oint_{\Lambda^3}^{N}|\mathscr{J}^e_\kappa|\left[\tilde{\nabla}\mathbf{v}^{\kappa,e}:\boldsymbol{\Upsilon}^{\kappa,e}:\tilde{\nabla}\mathbf{w}^{\kappa,e}\right](\boldsymbol{\xi})\\&+\sum_{\kappa=1}^{K}\sum_{e=1}^{n_\kappa}\oint_{\Lambda^3}^{N}|\mathscr{J}^e_\kappa|\left[\rho^{\kappa,e}\mathrm{Sym}\left\{\bar{w}^{\kappa,e}\tilde{\nabla}\cdot\mathbf{v}^{\kappa,e}-\mathbf{v}^{\kappa,e}\cdot\tilde{\nabla}\bar{w}^{\kappa,e}\right\}\right](\boldsymbol{\xi}),\end{aligned} \tag{B.14}$$

where the notation $\bar{w}$ stands for the scalar product $\mathbf{g}\cdot\mathbf{w}$.

To derive the approximated bilinear form $\mathscr{B}^{\mathrm{S}}_{\mathrm{h}}$ we recall the definition of $\mathscr{B}^{\mathrm{S}}$ given by (43):

$$\mathscr{B}^{\mathrm{S}}(\mathbf{w},\boldsymbol{\mu}) = \sum_{\underline{\kappa}=1}^{\underline{K}} \sum_{e=1}^{n_{\underline{\kappa}}} \int_{\upsilon^e_{\underline{\kappa}}} \left(\mathbf{w}_{\underline{\kappa}} - \mathbf{w}_{\kappa'}\right) \cdot \boldsymbol{\mu}_{\underline{\kappa}} \, \mathrm{d}\Gamma.$$

Note that both $\boldsymbol{\mu}_{\underline{\kappa}}$ and $\mathbf{w}_{\underline{\kappa}}$ are defined on the same quadrangles, unlike $\mathbf{w}_{\kappa'}$ which is defined on the coarser grid $\boldsymbol{\upsilon}_{\kappa'}$. For a given quadrangle $\upsilon^e_{\underline{\kappa}}$, let us denote by $a(e)$ the set of indices such that:

$$\forall a \in a(e), \quad \upsilon^a_{\kappa'} \cap \upsilon^e_{\underline{\kappa}} \neq \emptyset. \tag{B.15}$$

On $\upsilon^e_{\underline{\kappa}} \cap \upsilon^a_{\kappa'}$ the following trivial equality holds:

$$\mathbf{w}_{\kappa'}|\upsilon^e_{\underline{\kappa}} = \mathbf{w}_{\kappa'}|\upsilon^a_{\kappa'}. \tag{B.16}$$

This can also be expressed as:

$$\mathbf{w}_{\kappa'}|\upsilon^e_{\underline{\kappa}} = \mathbf{w}^{\kappa',a} \circ \left(\mathscr{G}^a_{\kappa'}\right)^{-1}, \tag{B.17}$$

which is desirable since $\mathbf{w}^{\kappa',a}$ is defined as a polynomial on the unit square Λ^2. Then, expressing the integrals of (43) back onto the unit square and making use of numerical integration yields:

$$\mathscr{B}^{\mathrm{S}}_{\mathrm{h}}(\mathbf{w},\boldsymbol{\mu}) = \sum_{\underline{\kappa}=1}^{\underline{K}} \sum_{e=1}^{n_{\underline{\kappa}}} \sum_{a=1}^{a(e)} \oint_{\Lambda^2}^{N} |\mathscr{J}^e_{\underline{\kappa}}| \left[\left(\mathbf{w}^{\underline{\kappa},e} - \underline{\Pi}^{\underline{\kappa},e}\mathbf{w}^{\kappa',a}\right) \cdot \boldsymbol{\mu}^{\underline{\kappa},e}\right](\boldsymbol{\xi}), \tag{B.18}$$

where we have denoted:

$$\underline{\Pi}^{\underline{\kappa},e}\mathbf{w}^{\kappa',a} \doteq \mathbf{w}^{\kappa',a} \circ \left[\left(\mathscr{G}^a_{\kappa'}\right)^{-1} \circ \mathscr{G}^e_{\underline{\kappa}}\right], \tag{B.19}$$

and where $|\mathscr{J}^e_{\underline{\kappa}}|$ stands for the Jacobian of the 2D transformation $\mathscr{G}^e_{\underline{\kappa}}$.

To compute the jump matrix two steps are thus required. First, the topology of the non-matching grids has to be detailed through the sets of indices $a(e)$ defined by (B.15). Second, the expression of the mapping local to the unit square $\left[\left(\mathscr{G}^a_{\kappa'}\right)^{-1} \circ \mathscr{G}^e_{\underline{\kappa}}\right]$ has to be provided before to perform the numerical integration. Both steps are quite straightforward to achieve, especially for simple grids where a coarsening of a factor of two is considered in each direction of space.

References

[1] B. Romanowicz, Seismic tomography of the Earth's mantle, Ann. Rev. Earth Planet. Sci. 19 (1991) 77–99.
[2] M.H. Ritzwoller, E.M. Lavely, Three dimensional seismic models of the Earth's mantle, Rev. Geophys. 33 (1995) 1–66.
[3] F.A. Dahlen, J. Tromp, Theoretical Global Seismology, Princeton University Press, Princeton, NJ, 1998.
[4] P. Lognonné, E. Clévédé, Normal modes of the earth and planets, in: P. Jennings, H. Kanamori, W. Lee (Eds.), Handbook of Earthquake and Engineering Seismology, vol. 1, IASPEI, Paolo Alto, CA, 2002, Part II-10.
[5] I. Gelfand, R. Minlos, Z. Shapiro, Representations of the rotation group and Lorentz groups and their applications, MacMillan, New York, 1963.
[6] E. Newman, R. Penrose, Note on the Bondi–Metzner–Sachs group, J. Math. Phys. 7 (1966) 836.
[7] R.A. Phinney, R. Burridge, Representation of elastic-gravitational excitation of a spherical Earth model by generalized spherical harmonics, Geophys. J. R. Astron. Soc. 34 (1973) 451–487.
[8] T. Wu, C. Yang, Some properties of monopole harmonics, Phys. Rev. D 16 (1977) 1018.
[9] B. Valette, Spectre des oscillations libres de la Terre: aspects mathématiques et géophysiques, Thèse de Doctorat d'état, Université Paris VII, 1987.

[10] P. Lognonné, Normal modes and seismograms in an anelastic rotating earth, J. Geophys. Res. 96 (1991) 20309–20319.
[11] P. Lognonné, E. Clévédé, Diffraction of long-period Rayleigh waves by a slab: effects of mode coupling, Geophys. Res. Lett. 24 (1997) 1035–1038.
[12] E. Clévédé, C. Mégnin, B. Romanowicz, P. Lognonné, Seismic waveform modeling and surface wave tomography in a three-dimensional Earth: asymptotic and non-asymptotic approaches, Phys. Earth Planet. Int. 119 (2000) 37–56.
[13] B. Romanowicz, Multiplet–multiplet coupling due to lateral heterogeneity: asymptotic effects on the amplitude and frequency of the Earth's normal modes, Geophys. J. R. Astron. Soc. 90 (1987) 75–100.
[14] X.D. Li, B. Romanowicz, Comparison of global waveform inversions with and without considering cross–branch modal coupling, Geophys. J. Int. 121 (1995) 695–709.
[15] J. Tromp, F.A. Dahlen, Variational principles for surface wave propagation on a laterally heterogeneous Earth: 2. Frequency domain JWKB theory, Geophys. J. Int. 109 (1992) 599–619.
[16] R. Snieder, B. Romanowicz, A new formalism for the effect of lateral heterogeneity on normal modes and surface waves: I. Isotropic perturbations, perturbations of interfaces and gravitational perturbances, Geophys. J. Int. 92 (1988) 207–222.
[17] F. Pollitz, Scattering of spherical elastic waves from small-volume spherical inclusion, Geophys. J. Int. 134 (1998) 390–408.
[18] W. Friederich, Propagation of seismic shear and surface waves in a laterally heterogeneous mantle by multiple forward scattering, Geophys, J. Int., 1998.
[19] W. Friederich, J. Dalkolmo, Complete synthetic seismograms for a spherically symmetric Earth by a numerical computation of the Green's function in the frequency domain, Geophys. J. Int. 122 (1995) 537–550.
[20] R.J. Geller, T. Ohminato, Computation of synthetic seismograms and their partial derivatives for heterogeneous media with arbitrary natural boundary conditions using the Direct Solution Method, Geophys. J. Int. 116 (1994) 421–446.
[21] R.J. Geller, N. Takeuchi, A new method for computing highly accurate DSM synthetic seismograms, Geophys. J. Int. 123 (1995) 449–470.
[22] P.N. Swarztrauber, Spectral transform methods for solving the shallow water equations on the sphere, Mon. Weather Rev. 124 (1996) 730–744.
[23] H. Igel, M. Weber, *SH*-wave propagation in the whole mantle using high-order finite differences, Geophys. Res. Let. 22 (1995) 731–734.
[24] E. Chaljub, A. Tarantola, Sensitivity of *SS* precursors to topography on the upper-mantle 660-km discontinuity, Geophys. Res. Lett. 24 (1997) 2613–2616.
[25] T. Furumura, B.L.N. Kennett, H. Takenaka, Parallel 3-D pseudospectral simulation of seismic wave propagation, Geophysics 63 (1998) 279–288.
[26] T. Furumura, B.L.N. Kennett, M. Furumura, Seismic wavefield calculation for laterally heterogeneous whole Earth models using the pseudospectral method, Geophys. J. Int. 135 (1998) 845–860.
[27] R. Sadourny, Conservative finite-difference approximations of the primitive equation on quasi-uniform spherical grids, Mon. Weather Rev. 100 (1972) 136–144.
[28] R. Heikes, D.A. Randall, Numerical integration of the shallow-water equations on a twisted icosahedral grid. Part I: basic design and results of tests, Mon. Weather Rev. 123 (123) (1995) 1862–1880.
[29] R. Heikes, D.A. Randall, Numerical integration of the shallow-water equations on a twisted icosahedral grid. Part II: a detailed description of the grid and an analysis of numerical accuracy, Mon. Weather Rev. 123 (123) (1995) 1881–1887.
[30] M. Rančić, R.J. Purser, F. Mesinger, A global shallow-water model using expanded spherical cube: gnomonic versus conformal coordinates, Quart. J. R. Met. Soc. 122 (1996) 959.
[31] C. Ronchi, R. Ianoco, P.S. Paolucci, The 'Cubed Sphere': a new method for the solution of partial differential equations in spherical geometry, J. Comput. Phys. 124 (1996) 93–114.
[32] G. Starius, On composite mesh difference methods for hyperbolic differential equations, Numer. Math. 35 (1980) 241–255.
[33] K.R. Kelly, R.W. Ward, S. Treitel, R.M. Alford, Synthetic seismograms: a finite difference approach, Geophysics 41 (1976) 2–27.
[34] M.A. Dablain, The application of high-order differencing to the scalar wave equation, Geophysics 51 (1986) 54–66.
[35] B. Fornberg, A practical guide to Pseudospectral methods, Cambridge University Press, New York, 1996.
[36] B. Fornberg, The pseudospectral method: accurate representation of interfaces in elastic wave calculations, Geophysics 53 (1988) 625–637.
[37] D. Kosloff, H. Tal-Ezer, A modified Chebyshev pseudospectral method with an $O(N^{-1})$ time step restriction, J. Comput. Phys. 104 (1993) 457–469.
[38] A.T. Patera, A spectral element method for fluid dynamics: laminar flow in a channel expansion, J. Comput. Phys. 54 (1984) 468–488.
[39] Y. Maday, A.T. Patera, Spectral element methods for the incompressible Navier–Stokes equations, in: A.K. Noor, J.T. Oden (Eds.), State of the Art Survey in Computational Mechanics, ASME, New York, 1989, pp. 71–143.

[40] C. Bernardi, Y. Maday, Approximations spectrales de problèmes aux limites elliptiques, Springer-Verlag, Paris, 1992.
[41] E. Priolo, J.M. Carcione, G. Seriani, Numerical simulation of interface waves by high-order spectral modeling techniques, J. Acoust. Soc. Am. 95 (2) (1994) 681–693.
[42] E. Faccioli, F. Maggio, A. Quarteroni, A. Tagliani, Spectral-domain decomposition methods for the solution of acoustic and elastic wave equations, Geophysics 61 (4) (1996) 1160–1174.
[43] E. Faccioli, F. Maggio, R. Paolucci, A. Quarteroni, 2D and3D elastic wave propagation by a pseudospectral domain decomposition method, J. Seismol. 1 (1997) 237–251.
[44] D. Komatitsch, J.-P. Vilotte, The spectral element method: an effective tool to simulate the seismic response of 2D and 3D geological structures, Bull. Seismol. Soc. Am. 88 (1998) 368–392.
[45] D. Komatitsch, J.-P. Vilotte, R. Vai, J.M. Castillo-Covarrubias, F.J. Sánchez-Sesma, The spectral element method for elastic wave equations – application to 2-D and 3-D seismic problems, Int. J. Numer. Meth. Eng. 45 (1998) 1139–1164.
[46] S.A. Orszag, Spectral methods for problems in complex geometries, J. Comp. Phys. 37 (1980) 70–92.
[47] A. Bermúdez, R. Rodríguez, Finite element computation of the vibration modes of a fluid–solid system, Comput. Methods Appl. Mech. Eng. 119 (1994) 355–370.
[48] L.L. Thompson, P. Pinsky, A space-time finite element method for structural acoustics in infinite domains, Comput. Methods Appl. Mech. Eng. 132 (1996) 195–227.
[49] D. Komatitsch, C. Barnes, J. Tromp, Wave propagation near a fluid–solid interface: a spectral element approach, Geophysics 65 (2) (2000) 623–631.
[50] D. Komatitsch, J. Tromp, Spectral-element simulations of global seismic wave propagation, Part I: validation, Geophys. J. Int. 149 (2002) 390–412.
[51] B. Valette, Spectre des vibrations propres d'un corps élastique, auto-gravitant, en rotation uniforme et contenant une partie fluide, C. R. Acad. Sci. Paris 309 (Série I) (1989) 419–422.
[52] E. Chaljub, Modélisation numérique de la propagation d'ondes sismiques en géométrie sphérique: application à la sismologie globale [Numerical modeling of seismic wave propagation in spherical geometry: application to global seismology], Ph.D. Thesis, Université Denis Diderot, Paris VII, 2000.
[53] Y. Capdeville, E. Chaljub, J.-P. Vilotte, J.-P. Montagner, Coupling the spectral element method with a modal solution for elastic wave propagation in global earth models, Geophys. J. Int. 152 (2003) 34–67.
[54] T.G. Cowling, The non-radial oscillations of polytropic stars, Mon. Not. R. Astron. Soc. 101 (1941) 369–373.
[55] C. Bernardi, Y. Maday, A.T. Patera, A new nonconforming approach to domain decomposition: the mortar element method, in: H. Brezis, J.L. Lions (Eds.), Nonlinear Partial Differential Equations and Their Applications, Pitman and Wiley, New York, 1994, pp. 13–51.
[56] F. Ben Belgacem, The mortar finite element method with Lagrange multipliers, Numer. Math. 84 (1999) 173–197.
[57] L.D. Landau, E.M. Lifschitz, Fluid Mechanics, Pergamon Press, Oxford, England, 1959.
[58] J.P. Cox, Theory of Stellar Pulsation, Princeton University Press, Princeton, NJ, 1980.
[59] P.A. Raviart, J.-M. Thomas, Primal hybrid finite element methods for 2nd order elliptic equations, Math. Comput. 31 (1977) 391–413.
[60] B. Valette, About the influence of pre-stress upon the adiabatic perturbations of the Earth, Geophys. J. R. Astron. Soc. 85 (1986) 179–208.
[61] M. Taylor, J. Tribbia, M. Iskandarani, The spectral element method for the shallow water equations on the sphere, J. Comp. Phys. 130 (1997) 92–108.
[62] C. Farhat, F.X. Roux, A method of Finite Element Tearing and Interconnecting and its parallel solution, Int. J. Num. Meth. Eng. 32 (1991) 1205–1227.
[63] C. Lacour, Y. Maday, Two different approaches for matching nonconforming grids: the Mortar Element method and the FETI method, BIT Numer. Math. 37 (3) (1997) 720–738.
[64] T.J.R. Hugues, The Finite Element Method, Linear Static and Dynamic Finite Element Analysis, Prentice-Hall International, 1987.
[65] P. Fischer, Analysis and application of a parallel spectral element method for the solution of the Navier–Stokes equations, Comp. Meth. Appl. Mech. Eng. 80 (1990) 483–491.
[66] H. Takeuchi, M. Saito, Seismic surface waves, Meth. Comp. Phys. 11 (1972) 217–295.
[67] J.H. Woodhouse, The calculation of eigenfrequencies and eigenfunctions of the free oscillations of the Earth and the Sun, in: D.J. Doornbos (Ed.), Seismological Algorithms, Academic Press, New York, 1988, pp. 321–370.
[68] M. Saito, DISPER80: A subroutine package for the calculation of seismic normal-mode solutions, in: D.J. Doornbos (Ed.), Seismological Algorithms, Academic Press, New York, 1988, pp. 294–319.
[69] G. Seriani, E. Priolo, Spectral element method for acoustic wave simulation in heterogeneous media, Finite Elem. Anal. Des. 16 (1994) 337–348.
[70] B. Rulf, Rayleigh waves on curved surfaces, J. Acoust. Soc. Am. 45 (1969) 493–499.

[71] N. Jobert, R. Gaulon, A. Dieulin, G. Roult, Sur les ondes de très longue période, caractéristiques du manteau supérieur, C. R. Acad. Sci. Paris Série B 285 (1977) 49–51.
[72] J.N. Brune, J.E. Nafe, L.E. Alsop, The polar phase shift of surface waves on a sphere, Bull. Seismol. Soc. Am. 51 (1961) 247–257.
[73] Z. Wang, F.A. Dahlen, J. Tromp, Surface-wave caustics, Geophys. J. Int. 114 (1993) 311–324.
[74] G. Masters, Observational constraints on the chemical and thermal structure of the Earth's interior, Geophys. J. R. Astron. Soc. 57 (1979) 507–534.
[75] C. Canuto, M.Y. Hussaini, A. Quarteroni, T.A. Zang, Spectral Methods in Fluid Dynamics, Springer, Berlin, 1987.